IEEE Access
Multidisciplinary | Rapid Review | Open Access Journal

Received 17 May 2023, accepted 29 June 2023, date of publication 7 July 2023, date of current version 14 July 2023.

*Digital Object Identifier 10.1109/ACCESS.2023.3293399*

RESEARCH ARTICLE

# A Novel Catchment Estimation for Super-Resolution DEM With Physically Based Algorithms: Surface Water Path Delineation and Specific Catchment Area Calculation

**AJALAWIT CHANTAVEEROD[1], KAMPOL WORADIT[2], (Member, IEEE), ANDREW SEAGAR[3], (Senior Member, IEEE), AND THUNYAWAT LIMPITI[1], (Member, IEEE)**

[1]Center of Excellence in Sustainable Disaster Management, Department of Electrical Engineering, School of Engineering and Technology, Walailak University, Nakhon Si Thammarat 80161, Thailand
[2]Optimized AI Systems for Energy and Environmental Sustainability Research Group, Department of Computer Engineering, Faculty of Engineering, Chiang Mai University, Chiang Mai 50200, Thailand
[3]School of Engineering and the Built Environment, Griffith University, Gold Coast Campus, Southport, QLD 4222, Australia

Corresponding author: Kampol Woradit (kampol.w@cmu.ac.th)

This work was supported in part by the Center of Excellence in Sustainable Disaster Management (CESDM) funded by the Agricultural Research Development Agency (Public Organization) under Grant PRP6405032390, and in part by Chiang Mai University.

**ABSTRACT** Hydrologists usually gain insights into topographic variability by using a high-performance algorithm to estimate the catchment area from a digital elevation model (DEM) image. In the literature, the grid-based algorithms are more popular than the contour-based algorithms; however, the existing ones cannot reduce the error when higher resolution DEM is available. This paper introduces a new contour-based algorithm, formulated with the physically-based concept, to estimate catchment from contour-based DEM data. The formulation was derived from the semi-analytical solution of Laplace's partial differential equation based on the boundary element method (BEM). With this approach, the algorithm can estimate the catchment area along the smooth surface water paths (SWPs), which are delineated from the physically-based algorithm. The proposed algorithm was validated with the standard synthetic surfaces, where the theoretical specific catchment areas (SCAs) for error assessment are exactly known. When estimating the SCAs with ordinary resolution, the average error of the estimated SCAs is between 14.19 and 2.32%, but the average error from the popular grid-based algorithms is between 77.8 and 17.0 %. With higher resolutions, between 12.5 and 0.88 meters, the proposed algorithm significantly reduces the average error from 15 to 0.8%.

**INDEX TERMS** Digital elevation model (DEM), boundary element method (BEM), catchment estimation, physically-based algorithms.

## I. INTRODUCTION

The size of the catchment is the principal value for analyzing the hydrological response of the catchment system [2] because the catchment collects the amount of rainwater and melted snow from ridgelines over higher areas into a single water body. Moreover, the effective catchment area has become a significant factor in various applications, for example, seasonal water availability assessment [3], water resources management [4], [5], [6], flood risk management [7], and water quality controls [8]. Therefore, the accuracy of the catchment estimation influences a variety of hydrological models, including a model for forecasting urban floods [9]. However, the current catchment estimation over a wide area inevitably has a residual error that cannot be mitigated without the physically-based algorithm [10], [11].

The associate editor coordinating the review of this manuscript and approving it for publication was Yizhang Jiang.

The researchers started developing models for estimating catchment since surface elevation data were available from the digital elevation model (DEM). To estimate a catchment, the researchers have utilized the DEM data in grid-based and contour-based forms [12]. Technologies of geographic information systems and remote sensing help us improve the quality of DEM from low-resolution [13], [14] to super-resolution [15]. Then, many researchers expected that the existing catchment estimation could give more accurate results when exploiting high-resolution DEM. For example, Li [10] used existing grid-based methods to delineate catchment boundaries with artificial super-resolution DEM. Surprisingly, both of them did not obtain better accuracy. This indicates that grid-based methods do not extract important topographic variabilities such as total dispersion area (TDA), topographic wetness index (TWI), and total contributing area (TCA) [16] from high-resolution DEM.

Governments worldwide have been aware that their people suffer from flood disasters since the extreme effects of climate and land use changes seem to intensify. To manage the flood risk, hydrologists must estimate the catchment to calculate the rainwater flow rate from the natural terrain into the city. For example, [11] proposed a hybrid method that separately considers the natural terrain areas in the first-level catchment and the urban area in the second-level catchment. Hydrologists employ conventional catchment estimation and raw topographic data to estimate the first-level catchment. Next, they use the estimated catchment at the first level as the primary data for analyzing artificial drainage systems and flow direction. In the case of a small and single catchment, the existing catchment estimations are reliable tools for understanding the effect of land use or land-cover change on stream runoff dynamic [17]. However, these tools cannot give less error in complicated or hybrid catchments, which contain a problematic flat terrain between natural and city areas. Therefore, the accuracy of the first-level catchment is the critical factor in improving the calculation of the flow rate of rainwaters flowing into the urban, especially on a larger scale [18]. Hence, this work aims to improve the accuracy of the catchment estimation over the sizeable natural terrain area.

Developing the DEM-based catchment estimation is categorized into grid-based, contour-based, and TIN-based (Triangulated Irregular Network) methods [19], [20]. The DEM grid-based methods that exploit the D8 algorithms to delineate the surface water flow are simple and require fewer computational resources [21], [22]. Since DEMs are available, the DEM grid-based methods have been prevalent. Unfortunately, using high-resolution DEMs in D8-based algorithms does not improve accuracy [23], [24], [25], [26]. Moreover, using super-resolution DEMs does not help D8-based algorithms to improve accuracy [27]. Recently, [10] evaluated the accuracy of six enhanced D8-based algorithms, namely Rho4, Rho8, D8-LTD, FDFM, DEMON, and D$\infty$, and their results indicate that the average area error ranges from 16.3% to 75.2%. The major limitation of the enhanced D8-based methods is the division of the catchment with non-physically-based surface water path in the downstream direction, which is calculated from the elevation difference between one central grid and its eight adjacent grids instead of the water movement concept.

On the other hand, the DEM contour-based methods in the physically-based concept are suitable for hydrological applications, and other geophysical processes [19], [28]. An essential step in all contour-based catchment estimation methods is the delineation of surface water path (SWP) between adjacent contour lines. The accuracy of SWP positions extracted from a DEM image influences the precision of the estimated catchment. In [29] and [30], the gravity-driven movements of water and sediments are considered in delineating a series of SWP segments between adjacent contour lines. They can eliminate the spurious SWPs found in grid-based algorithms. With the algorithm's effectiveness, many hydrologists, who need to estimate a sub-catchment area based on SWP, implemented this algorithm in the catchment model [31], [32]. However, when SWP is delineated near a ridge, this algorithm must be done manually. Accordingly, [33] automates this algorithm by improving robustness when SWPs are delineated near a ridge. The paper [34] further improves the SWP smoothness by including skeleton construction techniques, but this method loses the smoothness advantage when the distance between adjacent contour lines is long. Nevertheless, when all mentioned contour-based methods are used in complex terrains such as a saddle over a large area, very high computational resources are required because many grids and unknown variables in spatial discretization between contour lines represent that area. Moreover, estimating catchment area from smooth SWPs demands enormous computational resources [35]. In [1], the physically and BEM (Boundary Element Method)-based SWP delineation algorithm is proposed to improve the accuracy of SWP delineation from high-resolution DEMs with inexpensive computational resources. In the next step, the obtained SWPs can be used to estimate catchment size parameters in the hydrological model. Existing estimation algorithms are available in the grid-based approach, which suffers an error floor even though the resolution becomes higher [10]. This inspires us to propose a different approach, which is physically and BEM-based. The proposed algorithm accurately estimates the catchment area from the delineated SWPs of [1] with affordable computational resources, especially at high DEM resolution.

Our proposed algorithm estimates catchment area by maintaining the advantages of a physically-based concept. In the first step, the unknown elevations at any points between adjacent contour lines are interpolated to identify the boundary of catchment area. Theoretically, the continuous integral-form solution of partial differential equation (Laplace's equation) gives the interpolation, but practically

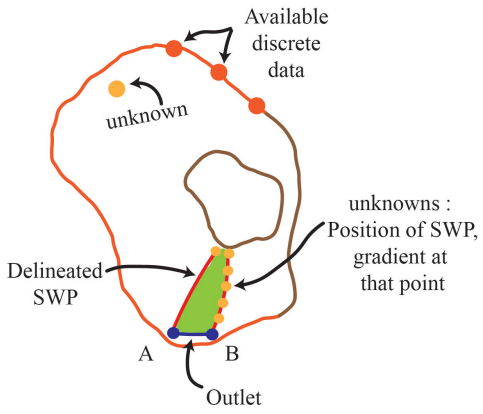


**FIGURE 1.** A differential catchment area (shaded area), where a line integral is calculated.

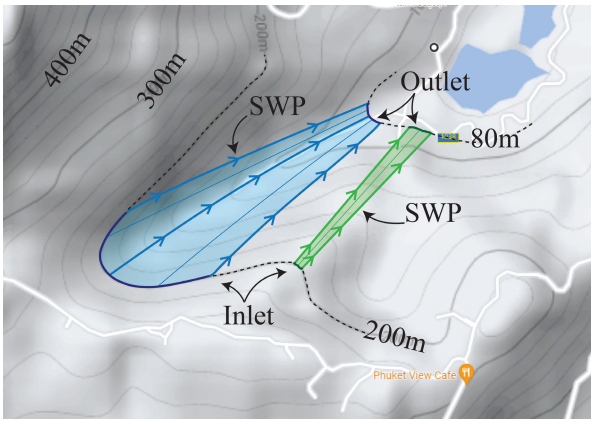


**FIGURE 2.** Boundary of catchment area.

available elevation data are discrete. Therefore, this algorithm replaces the integral-form solution by the boundary element method (BEM) in [1], which is a numerical solution that preserves SWP smoothness with affordable computational resources even in case of complex terrain. In the second step, the line integrals of hillslope (magnitude of gradient of the interpolated elevation) are calculated along all smooth SWPs (obtained by [1]'s algorithm) to estimate the lengths of differential catchment area. Note that each line integral starts from an outlet and ends at the hilltop. In the third step, the line integral of differential catchment area is calculated along the line of outlet to estimate catchment area as shown in Fig. 1. Straightforwardly, the high-resolution DEM is of great benefit to accuracy of line integrals in the second and the third steps. The comparison with existing algorithms shows that the proposed algorithm provides superior accuracy. Also, we will show that the catchment estimation accuracy can be further improved by using super-resolution DEM.

The remainder of this article is structured as follows. Section II proposes a new algorithm to estimate sub-catchment by autonomous partitioning of smooth SWPs, delineated with contour-based algorithm of [1]. Next, in Section III, we demonstrate and discuss the accuracy of the estimated catchment over standard synthetic surfaces with comparisons to existing algorithms. Last, we conclude the paper in Section IV.

## II. METHODS

This section presents the contour-based algorithm to estimate the catchment area. First, we propose the physically-based theory manipulating the theoretical catchment estimation. Second, we numerically calculate the catchment size with a line integral, where the outlet and the SWPs serve as the boundary of catchment. This work determines the positions of SWPs with the algorithm in [1]. Third, we calculate the hillslope at points along each SWP. The computation algorithm for the second and third steps will be given in the last subsection.

### A. THEORETICAL ESTIMATION OF CATCHMENT AREA

This section proposes the theoretical estimation of the catchment area. The size of the catchment area is the surface integral over the catchment area, bounded by a set of SWP positions, inlet, and outlet. Calculating the size of the catchment area with the surface integration uses the value of the hillslope, which is the analytical solution of Laplace's equation.

When the position of an outlet locating along a contour line, [1]'s algorithm can reversely predict the position of the surface water paths (SWPs) flowing from the outlet toward the inlet. Then, this work applies the SWP positions to identify the boundary of the catchment area and to calculate the integral of the catchment size function over the surface domain containing the positions of the fixed outlet and delineated SWPs. For example, Fig.2 presents two different catchment areas: the light green area and the light blue area. The outlet of the light green catchment area locates along the 80-m elevation line. Its delineated SWPs are light green and flow from a 200-m elevation line. The outlet of the light blue catchment area locates on the same line. Its delineated SWPs are light blue and flow from a 200-m elevation line. With the same width of the outlet, the blue catchment area is wider than the green area because the blue SWPs are converging while the green SWPs are diverging. This means the size of the catchment area depends on the shape of the SWPs flowing from the inlet to the outlet.

In determining the catchment area's size, the surface integration domains are the contours' and SWPs' positions. The real contours and SWPs are very complex curves, not straight. Therefore, the analytical solution of Laplace's equation is often derived from the curvilinear coordinates $(s, t, v)$ instead of the cartesian coordinates $(x, y, z)$ as shown in Fig. 3. The notations $\mathsf{u}_j$ and $\mathsf{h}_i$ represent the $j^{th}$-SWP and the $i^{th}$-contour, respectively. For example, point $A$ is an intersection between SWP $\mathsf{u}_j$ and contour $\mathsf{h}_{i+1}$. The notation $ds$ defines an elementary arc length of the SWP segment from point $A$ to $D$, and the $dt$ defines an elementary arc length of the contour segment from point $A$ to $B$.

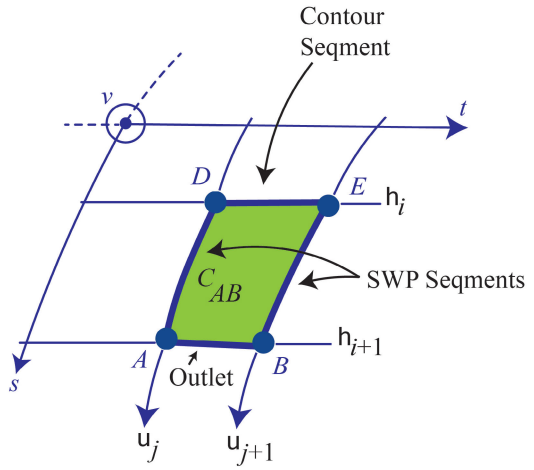


**FIGURE 3.** Contour and surface water path in curvilinear coordinate system.

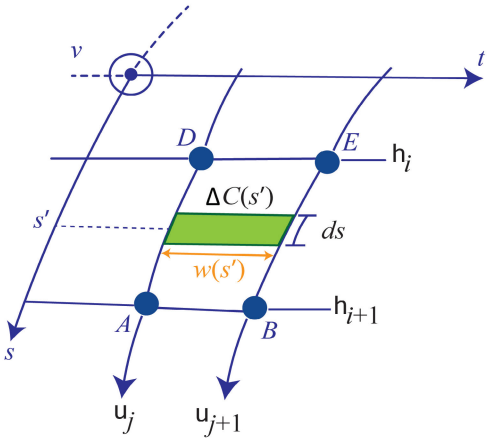


**FIGURE 4.** A segment of catchment area $\Delta C$.

### 1) LINE INTEGRAL FOR THEORETICAL CATCHMENT

Denote $C_{AB}$ as a theoretical catchment flowing into an outlet segment between points $A$ and $B$. To formulate the theoretical catchment $C_{AB}$, we first consider an outlet segment from point $A$ to point $B$ in the curvilinear coordinate system in Fig. 3. Second, after obtaining positions of SWPs flowing into the outlet from [1], we know the boundary of catchment $C_{AB}$. For example, the boundary of $C_{AB}$ comprises (i) the segment of contour line $h_{i+1}$ from point $A$ to $B$, (ii) the segment of SWP $u_{j+1}$ from $B$ to $E$, (iii) the segment of contour line $h_i$ from point $E$ to $D$, and (iv) the segment of SWP $u_j$ from $D$ to $A$.

Third, a width function, denoted by $w(s')$, gives the distance between SWPs $u_j$ and $u_{j+1}$ at $s = s'$. A multiplication between $w(s')$ and $ds$ gives an infinitesimal element of catchment area $\Delta C(s')$ as shown in Fig. 4. The size of the element $\Delta C(s')$ is given by

$$\Delta C(s') = w(s')ds. \tag{1}$$

Last, the size of catchment $C_{AB}$ can be calculated with line integral of the width function $w(s')$ along the $u_j$-SWP from point $A$ to $D$:

$$C_{AB} = \int_A^D w(s')\, ds. \tag{2}$$

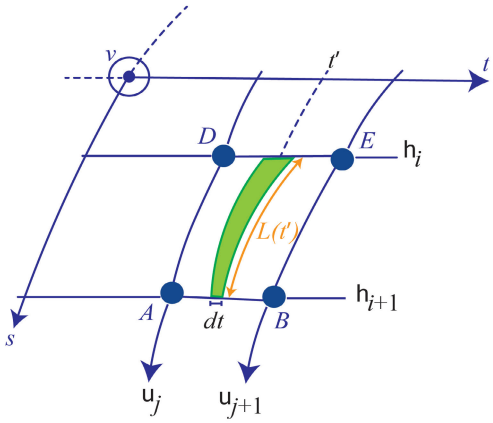


**FIGURE 5.** A differential catchment area $L(t')$.

To obtain the specific catchment area (SCA) referred by [23], we define the differential catchment area at $t = t'$ along the outlet from point $A$ to $B$. When considering an outlet with a width approaching zero, the rate of change of the catchment area $C_{AB}$ with respect to $t$ can be written as

$$L(t') = \left.\frac{dC_{AB}}{dt}\right|_{t=t'}, \tag{3}$$

and is referred to as a length function $L(t')$, which quantifies the distance between contours $h_i$ and $h_{i+1}$ at $t = t'$ as shown in Fig. 5. The size of catchment $C_{AB}$ can be calculated by line integral of length function $L(t')$ along contour $h_{i+1}$,

$$C_{AB} = \int_A^B L(t')\, dt. \tag{4}$$

### 2) CATCHMENT ESTIMATION WITH HILLSLOPE

To calculate the size of $C_{AB}$, we can use the line integral with either (2) or (4). This work selects the line integral in (2) because the width function $w(s')$ can be found from the known SWP positions, while the length function $L(t')$ is unknown. Then, we will define the width function of $w(s')$ in terms of the elevation gradient at point $s = s'$ along the SWP.

The elevation gradient can be found by applying the two-dimensional divergence theorem [36] at a point inside catchment $C_{AB}$.

$$\int_{C_{AB}} \nabla \cdot \nabla h(s,t)\, dc = \int_\Gamma \nabla h(s,t) \cdot \hat{n}\, d\gamma, \tag{5}$$

where $h(s,t)$ is the interpolated elevation function, and $dc$ is the differential area, and $\Gamma$ is the boundary of the catchment area, and $d\gamma$ is the differential length, and $\hat{n}$ is the outward normal unit vector at a point on boundary $\Gamma$. The left-hand side is a surface integral of $\nabla h(s,t)$ inside the catchment $C_{AB}$, and the right-hand side is a line integral of $\nabla h(s,t) \cdot \hat{n}$ along the boundary $\Gamma$ of catchment $C_{AB}$.

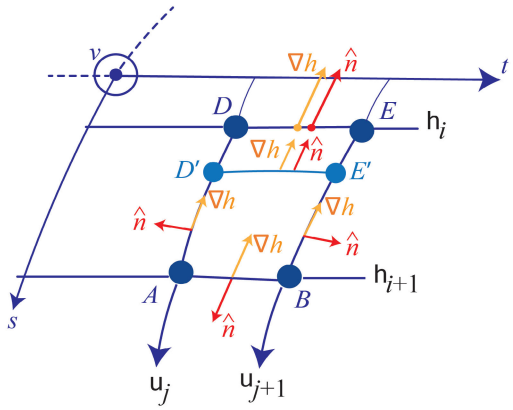


**FIGURE 6.** The boundary of catchment $C_{AB}$ for line integral.

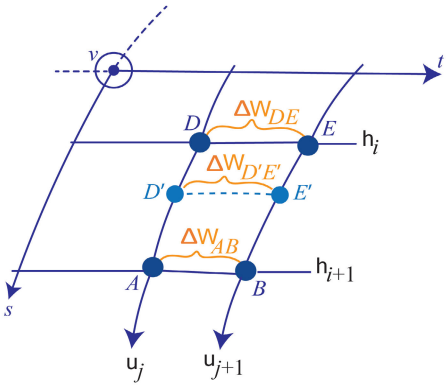


**FIGURE 7.** Changing inlet width.

In Fig. 6, the elevation gradient $\nabla h(s,t)$ can be considered as the solution of Laplace's equation $\nabla \cdot \nabla h(s,t) = 0$ in [1], so the left-hand side of (5) becomes zero. Then, integrating the right-hand side of (5) along the boundary of catchment $C_{AB}$ gives

$$\int_A^B \nabla h \cdot \hat{n}\, dt + \int_B^E \nabla h \cdot \hat{n}\, ds + \int_E^D \nabla h \cdot \hat{n}\, dt + \int_D^A \nabla h \cdot \hat{n}\, ds = 0. \tag{6}$$

Since $\nabla h$ are perpendicular to $\hat{n}$ along any SWP, the integrals from $B$ to $E$ and from $D$ to $A$ become zero. On the other hand, since $\nabla h$ are parallel to $\hat{n}$, the integrals from $A$ to $B$ and from $E$ to $D$ become $-|\nabla h|$ and $+|\nabla h|$, respectively. We obtain

$$-\int_A^B |\nabla h(P)| dt + \int_E^D |\nabla h(P')| dt = 0, \tag{7}$$

where $P$ denotes any point along segment $AB$ segment, and $P'$ denotes any point along segment $ED$.

If the segments of both line integrals are infinitesimal, $|\nabla h(P)|$ and $|\nabla h(P')|$ becomes constant, and we obtain

$$\begin{aligned} -|\nabla h(P)| \int_A^B ds + |\nabla h(P')| \int_E^D ds = 0, \\ -|\nabla h(P)| \Delta \mathsf{w}_{AB} + |\nabla h(P')| \Delta \mathsf{w}_{ED} = 0, \end{aligned} \tag{8}$$

where $\Delta \mathsf{w}_{AB}$ and $\Delta \mathsf{w}_{DE}$ denote the arc lengths of the contour line segments $AB$ and $ED$, respectively, as shown in Fig 7. Note that $B$ is infinitely close to $A$, and $E$ is infinitely close to $D$. Then, we can obtain the relationship between the width of the inlet segment $DE$ and the outlet segment $AB$.

$$\Delta \mathsf{w}_{DE} = \Delta \mathsf{w}_{AB} \frac{|\nabla h(A)|}{|\nabla h(D)|}. \tag{9}$$

We can apply the relationship between the inlet width and outlet width in (9) to move the inlet from segment $DE$ to an infinitely close inlet segment along an SWP. By moving the inlet to any segment $D'E'$ along the SWP as shown in Fig. 7, the inlet width changes from $\Delta \mathsf{w}_{DE}$ to

$$\Delta \mathsf{w}_{D'E'} = \Delta \mathsf{w}_{AB} \frac{|\nabla h(A)|}{|\nabla h(D')|}. \tag{10}$$

Substituting (9) into (2), we obtain the estimation of the differential catchment area at any point $A$ along the outlet $AB$:

$$\begin{aligned} \Delta C_{AB} &= \Delta \mathsf{w}_{AB} |\nabla h(A)| \int_A^D \frac{1}{|\nabla h(s)|} ds, \\ \frac{\Delta C_{AB}}{\Delta \mathsf{w}_{AB}} &= |\nabla h(A)| \int_A^D \frac{1}{|\nabla h(s)|} ds. \end{aligned} \tag{11}$$

Then, the differential catchment area at any point $P$ along the outlet $AB$ is denoted by $L(P)$, which is given by

$$L(P) = |\nabla h(P)| \int_A^D \frac{1}{|\nabla h(s)|} ds. \tag{12}$$

Finally, substituting (12) into (4), we obtain the size of catchment $C_{AB}$ by calculating line integral of $L(P)$ at any point $P$, which is along the outlet from point $A$ to $B$.

$$C_{AB} = \int_A^B L(P)\, dt. \tag{13}$$

### B. NUMERICAL ESTIMATION OF CATCHMENT AREA

To calculate the catchment size $C_{AB}$ in (13), we have to integrate the line integral of $L(P)$ along the outlet from point $A$ to $B$. Numerical integration is needed because of the contour-based DEM input, which is discrete-spatial. Also, we calculate the function $L(P)$ by evaluating the line integral of hillslope $|\nabla h|$ along discrete-spatial SWPs, which are obtained from [1].

Fig. 8 shows an integral domain, which is the outlet from point $A$ to $B$. The line integral of $L(P)$ in (13) is split into $(N_{\mathrm{SWP}} - 1)$ definite integrals, each of which is indexed by $j = 1 \ldots N_{\mathrm{SWP}} - 1$. Each interval is $[P_j, P_{j+1}]$, which is along the outlet from point $A$ to $B$. Note that point $P_j$ and $P_{j+1}$ are the points intersecting with the SWPs $\mathsf{u}_j$ and $\mathsf{u}_{j+1}$, respectively.

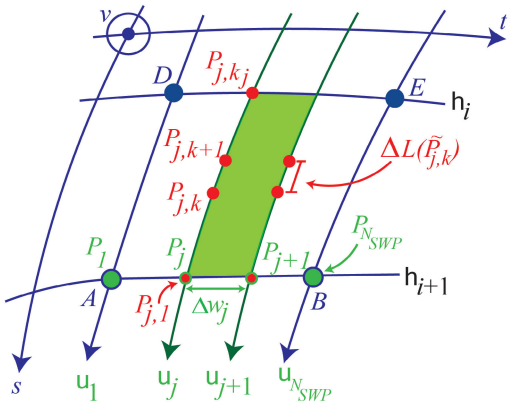


**FIGURE 8.** A subdomain for numerical integration of $C_{AB}$ and a subdomain for numerical integration of $L(P)$.

Then, the numerical integration is given by

$$C_{AB} = \sum_{j=1}^{N_{\mathrm{SWP}}-1} \int_{P_j}^{P_{j+1}} L(P)ds. \tag{14}$$

We approximate all definite integrals with Trapezoid method and obtain

$$C_{AB} = \sum_{j=1}^{N_{\mathrm{SWP}}-1} \Delta C(P_j) \tag{15}$$

where $\Delta C(P_j)$ is the $j^{th}$ element of catchment area at point $P_j$, which is given by

$$\Delta C(P_j) = \frac{\Delta \mathsf{w}_j}{2}\left[L(P_j) + L(P_{j+1})\right], \tag{16}$$

where $\Delta \mathsf{w}_j$ denotes the Euclidean distance between points $P_j$ and $P_{j+1}$. Finally, we obtain the catchment $C_{AB}$ in term of $L(P_j)$:

$$C_{AB} = \sum_{m=1}^{N_{\mathrm{SWP}}-1} \frac{\Delta \mathsf{w}_j}{2}\left[L(P_j) + L(P_{j+1})\right]. \tag{17}$$

Next, we calculate $L(P_j)$ in (17) with the integration of (12). Fig. 8 shows an integral domain, which includes the SWP positions from outlet $AB$ to inlet $DE$. The line integral of $\left|\nabla h(\tilde{P}_{j,k})\right|$ is split into $K_j - 1$ definite integrals, each of which is indexed by $k = 1 \ldots K_j - 1$ and $\tilde{P}_{j,k}$, $k = 1 \ldots K_j$ denotes a split point. Each interval is $[\tilde{P}_{j,k}, \tilde{P}_{j,k+1}]$, which is along the SWP $\mathsf{u}_j$. Note that the number of intervals of each SWP is not necessarily equal, that is, $K_j \neq K_{j+1}$ because of different SWP lengths or number of SWP positions. Then, the numerical integration is given by

$$L(P_j) = \sum_{k=1}^{K_j-1} \int_{\tilde{P}_{j,k}}^{\tilde{P}_{j,k+1}} \frac{G_j}{\left|\nabla h(\tilde{P}_{j,k})\right|} ds, \tag{18}$$

where $G_j = \left|\nabla h(\tilde{P}_{j,k=1})\right|$. We approximate all definite integrals with Trapezoid method and obtain

$$L(P_j) = \sum_{k=1}^{K_j-1} \Delta L(\tilde{P}_{j,k}) \tag{19}$$

where $\Delta L(\tilde{P}_{j,k})$ is the $k^{th}$ element of the differential catchment area at point $P_{i,k}$, which is given by

$$\Delta L(\tilde{P}_{j,k}) = \frac{G_j \Delta \mathsf{l}_k}{2}\left[\frac{1}{\left|\nabla h(\tilde{P}_{j,k})\right|} + \frac{1}{\left|\nabla h(\tilde{P}_{j,k+1})\right|}\right], \tag{20}$$

where $\Delta \mathsf{l}_k$ denotes the Euclidean distance between points $\tilde{P}_{j,k}$ and $\tilde{P}_{j,k+1}$, and the hillslope $\left|\nabla h(\tilde{P}_{j,k})\right|$ will be calculated in the next subsection.

### C. CALCULATION OF THE GRADIENT OF INTERPOLATED ELEVATION

For computational efficiency, the hillslope should be calculated only at the points $\tilde{P}_{j,k}$ that is used in (19). Therefore, this paper uses the algorithm in [1], which can specify a point to obtain the hillslope. Note that a point $\tilde{P}_{j,k}$ is between the contours $\mathsf{h}_i$ and $\mathsf{h}_{i+1}$ as shown in Fig.8.

In [1], the elevation gradient $\nabla h(P)$ is the solution of the boundary integral equation, which is formulated from Laplace's equation and boundary integral equation method, and can be expressed as

$$2\pi \nabla h(P) = \int_C \vec{A}(P, Q)\left(\nabla H(Q) \cdot \hat{n}(Q)\right) dc - \int_C \vec{B}(P, Q) H(Q) dc, \tag{21}$$

where $Q$ represents the position of $dc$ along the contour, and the vector functions $\vec{A}(P, Q)$ and $\vec{B}(P, Q)$ are the shape functions of points $P$ and $Q$, and can be expressed as

$$\vec{A}(P, Q) = \frac{\overrightarrow{PQ}}{\left\|\overrightarrow{PQ}\right\|^2}, \tag{22}$$

$$\vec{B}(P, Q) = \frac{\hat{n}(\vec{Q})}{\left\|\overrightarrow{PQ}\right\|^2} - 2\frac{\overrightarrow{PQ} \cdot \hat{n}(\vec{Q})}{\left\|\overrightarrow{PQ}\right\|^4}\overrightarrow{PQ}, \tag{23}$$

and $H(Q)$ and $\nabla H(Q)$ are the boundary value function of point $Q$.

The solution (21) is continuous, but the input DEM is discrete. Accordingly, the numerical solution was formulated in Section IV-B in [1] with boundary element method. This numerical solution can interpolate the $\nabla h(P)$ by using the elevation data along the discrete contour lines. This paper rewrites the numerical solution to conform with the computer algorithm in Section II-D.

$$2\pi \nabla h(P) = \sum_{e=1}^{N_e} \int_{Q_e}^{Q_{e+1}} \vec{A}(P, Q)\left(\nabla H(Q) \cdot \hat{n}(Q)\right) dc - \sum_{e=1}^{N_e} \int_{Q_e}^{Q_{e+1}} \vec{B}(P, Q) H(Q) dc, \tag{24}$$

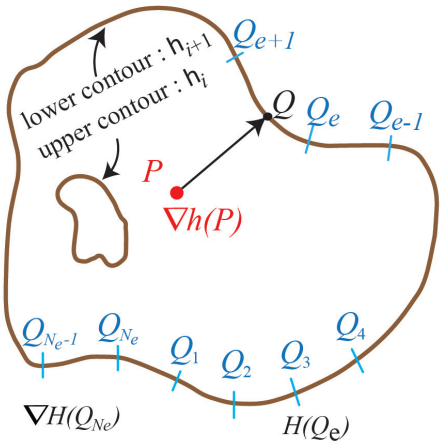


**FIGURE 9.** A subdomain for numerical integration of $\nabla h(P)$.

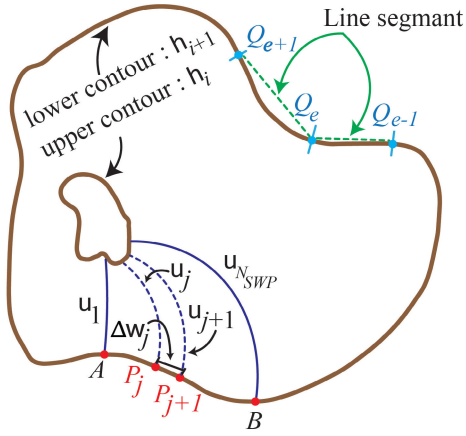


**FIGURE 10.** Chain of line segment.

where a contour representing discrete elevation data of $N_e+1$ is the domain for line integral, as shown in Fig. 9. The contour contains discrete elevation data of $N_e$, and each segment starts from $Q_e$ to $Q_{e+1}$. The boundary value functions $H(Q)$ and $\nabla H(Q)$ can be solved from DEM as shown in Section III in [1].

### D. ALGORITHM TO ESTIMATE CATCHMENT AREA

In this section, we propose a recursive algorithm for estimating a catchment area, which is the concatenation of several SWP segments over a catchment area, in which the elevation is represented with contour lines in a DEM image. The algorithm comprises four phases as follows.

#### 1) ALLOCATING THE MEMORY ON A COMPUTER

The first phase is to format the computer's memory to collect input and output data. The input data is a sequence of the sampled elevation data in a DEM image, which comprise three-dimensional coordinates of all contours. The open-source software packages such as QGIS [37] can generate the contour-based data by duplicating it from the contour-based DEM data or converting it from the grid-based DEM data. Each contour is represented with polylines (chain of line segments). The number of segments depends on the sampling rate. For example, Fig. 10 presents the elevation along two contour lines over a catchment area. The algorithm collects each coordinate, denoted by $Q_e$, on the contour lines $\mathsf{h}_i$ and $\mathsf{h}_{i+1}$.

#### 2) ASSIGNING THE OUTLET OF $C_{AB}$

To calculate the size of a catchment numerically with (14), we have to assign the starting point $A$ ($P_{j=1}$), and the endpoint $B$ ($P_{j=N_{\mathrm{SWP}}}$). Also, we designate $N_{\mathrm{SWP}}$, which is the number of the SWP so that the number of the catchment element equals $N_{\mathrm{SWP}}-1$. When increasing $N_{\mathrm{SWP}}$, the accuracy of the catchment estimation is higher at a cost of computational time. Any point $P_j$ along the outlet from point $A$ to $B$ intersects between the SWP $\mathsf{u}_j$ and the lower contour $\mathsf{h}_{i+1}$. We use the position of point $P_j$ as the starting point in delineating the SWP $\mathsf{u}_j$ from the lower contour $\mathsf{h}_{i+1}$ to the upper $\mathsf{h}_i$. Note that we delineate the SWP in the reverse direction because the result provides meaningful information for hydrological applications. The width of the outlet segment from $P_j$ to $P_{j+1}$ is $\Delta\mathsf{w}_j$, which equal $\|\overrightarrow{AB}\|/N_{\mathrm{SWP}}$. The $\Delta\mathsf{w}_j$ in $x$-component and $y$-component are denoted by $\Delta x_{\mathsf{w}_j}$ and $\Delta y_{\mathsf{w}_j}$, respectively.

#### 3) ITERATIVELY CALCULATING $\triangle C_j$

To estimate the size of a catchment numerically with (14), we have to use (16) to calculate $\Delta C_j$, which has the outlet segment from point $P_j$ to $P_{j+1}$. The position of $P_j$ is obtained from the previous phase. Each loop of $\Delta C_j$ calculation needs the values of $L(P_j)$ and $L(P_{j+1})$. Then, the number of the loops is $N_{\mathrm{SWP}}-1$, which is the number of the catchment elements.

#### 4) ITERATIVELY CALCULATING $\triangle L(\tilde{P}_{j,k})$

To estimate $L(P_j)$ numerically with (19), we have to loop through (20) to calculate $\Delta L(\tilde{P}_{j,k})$ from $k=1$ to $k=K_j$. For each loop, we must find the starting point of the $k^{th}$ SWP segment $\tilde{P}_{j,k}$ and the endpoint of the SWP segment $\tilde{P}_{j,k+1}$. To find both points for each loop, we follows Algorithm 2 to determine the starting point of the next SWP segment, which is presented in Section V in [1]. Looping is stopped when the endpoint touches or crosses the upper contour line.

All four phases can be written as pseudocodes as shown in Algorithm 1 and Algorithm 2, respectively.

## III. RESULTS AND DISCUSSIONS

This section demonstrates that the proposed algorithm can improve the accuracy of catchment estimation when the resolution of the elevation data is increased. For a fair comparison, this work follows the error assessment method proposed by [10]. The method applies the standard synthetic surfaces to measure the estimated catchment's errors. At the resolution available nowadays, the proposed algorithm can give more accuracy than the existing algorithms. In the future,

**Algorithm 1** An Algorithm to Estimate Catchment Area

**Input:** list of the zone's names in this catchment, list of the contour line's names in each zone, list of the point's coordinates along the contour lines

**Output:** the size of catchment area (meters): $C_{AB}$

*Initialisation* : $P_A \leftarrow (x_A, y_A)$; $P_B \leftarrow (x_B, y_B)$; $N_{\mathrm{SWP}} = 100$; $\mathsf{I}_{\mathsf{k}} \leftarrow 1.0$; $C_{AB} \leftarrow 0.0$;
$\Delta x_{\mathbf{w}_j} \leftarrow \|\overrightarrow{AB}\|/N_{\mathrm{SWP}}$ in $x$-component;
$\Delta y_{\mathbf{w}_j} \leftarrow \|\overrightarrow{AB}\|/N_{\mathrm{SWP}}$ in $y$-component;
*LOOP Process*
$j \leftarrow 1$;
$x_{P_j} \leftarrow x_{P_A}$;
$y_{P_j} \leftarrow y_{P_A}$;
**while** $j \leq (N_{\mathrm{SWP}} - 1)$ **do**
  $L(P_j) \leftarrow 0.0$;
  $k \leftarrow 1$;
  $\tilde{P}_{j,k=1} \leftarrow P_j$;
  **while** $(\tilde{P}_{j,k} \in \mathbb{C}_{AB})$ **do**
    **if** $k == 1$ **then**
      $\nabla h(\tilde{P}_{j,k}) \leftarrow$ Cal_Gradient$(\tilde{P}_{j,k})$ from (24);
      $\|\nabla h(\tilde{P}_{j,k})\| \leftarrow$ Find magnitude of $\nabla h(\tilde{P}_{j,k})$;
    **else**
      $\nabla h(\tilde{P}_{j,k+1}) \leftarrow$ Cal_Gradient$(\tilde{P}_{j,k+1})$ from (24);
      $\|\nabla h(\tilde{P}_{j,k+1})\| \leftarrow$ Find magnitude of $\nabla h(\tilde{P}_{j,k+1})$;
      compute $\Delta L(\tilde{P}_{j,k})$ from $\|\nabla h(\tilde{P}_{j,k})\|$, $\|\nabla h(\tilde{P}_{j,k+1})\|$ with (20);
      $L(P_j) \leftarrow L(P_j) + \Delta L(\tilde{P}_{j,k})$ with (19);
      $x_{\tilde{P}_{j,k}} \leftarrow x_{\tilde{P}_{j,k+1}}$;
      $y_{\tilde{P}_{j,k}} \leftarrow y_{\tilde{P}_{j,k+1}}$;
      $\nabla h(\tilde{P}_{j,k}) \leftarrow \nabla h(\tilde{P}_{j,k+1})$
    **end if**
    $\nabla^2 h(\tilde{P}_{j,k}) \leftarrow$ Cal_GradGrad$(\tilde{P}_{j,k})$ from (39);
    $\tilde{P}_{j,k+1} \leftarrow$ NEXT_Point$(\tilde{P}_{j,k})$ with Algorithm 2;
    $k = k + 1$;
  **end while**
  **if** $j == 1$ **then**
    $L(P_j) \leftarrow L(P_j)$;
  **else**
    $L(P_{j+1}) \leftarrow L(P_j)$;
    compute $\Delta C_j$ from $L(P_j)$, $L(P_{j+1})$ with (16);
    $C_{AB} \leftarrow C_{AB} + \Delta C(P_j)$ with (15);
    $L(P_j) \leftarrow L(P_{j+1})$;
  **end if**
  $x_{P_{j+1}} \leftarrow x_{P_j} + \Delta x_{\mathbf{w}_j}$;
  $y_{P_{j+1}} \leftarrow y_{P_j} + \Delta y_{\mathbf{w}_j}$;
  $j = j + 1$;
**end while**

when the super-resolution elevation data are available, the proposed algorithm can further reduce the error while the existing algorithms cannot.

**Algorithm 2** NEXT_Point$(\tilde{P}_{j,k})$

**Input:** $\tilde{P}_{j,k}$, $\nabla h(\tilde{P}_{j,k})$, $\nabla^2 h(\tilde{P}_{j,k})$, $\mathsf{I}_{\mathsf{k}}$

**Output:** $\tilde{P}_{j,k+1}$

$h_x \leftarrow$ Find $\nabla h(\tilde{P}_{j,k})$ in $x$-component;
$h_y \leftarrow$ Find $\nabla h(\tilde{P}_{j,k})$ in $y$-component;
$h_{xx} \leftarrow$ Find $\nabla^2 h(\tilde{P}_{j,k})$ in $xx$-component;
$h_{xy} \leftarrow$ Find $\nabla^2 h(\tilde{P}_{j,k})$ in $xy$-component;
Solve root:$\{\ \theta_{\min}, \theta_{\max}\ \}$ from (41);
$x_{\tilde{P}_{j,k+1}} \leftarrow x_{\tilde{P}_{j,k}} + r_0 \cos\theta_{\min}$;
$y_{\tilde{P}_{j,k+1}} \leftarrow y_{\tilde{P}_{j,k}} + r_0 \sin\theta_{\min}$;

### A. THEORETICAL SCAs OF SYNTHETIC SURFACE

Hydrologists use the catchment estimation algorithm to analyze the catchment and require continuous DEM data representing both measured and interpolated elevation data. Nevertheless, the developers commonly evaluate the algorithm's performance by varying the input data's scenarios, such as a pure hilltop, pure sink, and pure inclined plane [23]. Also, the developers measure the algorithm 's accuracy by referencing the exact value, which is the exact solution of the catchment estimation over an artificial surface [23], [38], [39]. Therefore, artificial surfaces are usually used to evaluate the actual performance of the catchment estimation algorithm. For example, the paper [10] applied the synthetic surfaces proposed by [23], namely ellipsoid surface, inverted ellipsoid surface, and inclined plane, for evaluating the accuracy of the existing grid-based algorithms. They measured the errors of the extracted SWPs and the estimated SCAs relative to the synthetic surfaces' theoretical values. They found that the D8 algorithm suffers from poor accuracy, and increasing the elevation data resolution cannot reduce the errors of the D8 algorithm and its extensions [10]. Later, the paper [1] applied the same assessment method on a contour-based algorithm and found that the contour-based algorithm can improve the accuracy of the extracted SWP positions. In assessment, synthetic surfaces have an advantage over real terrain DEMs because the analytical solutions derived from synthetic surface equations are unique [23], [38], [39]. Thus, this paper also uses the [23]'s surfaces to discuss the error assessment with [10]. We use the formulas of the mentioned surfaces to generate the elevation data and determine the errors with their theoretical SCAs. Moreover, we also adopt the synthetic surfaces proposed by [39], which reformulates the surfaces in [23] to make them close to realistic terrains.

For fair comparisons, we consider the same surfaces as [10]; namely, the ellipsoid, the inverted ellipsoid, and the inclined plane, proposed in [23], with the same parameters. In addition, the formulations in [39] are considered in case of ellipsoid and inverted ellipsoid to observe the results close to realistic terrains.

#### 1) ELLIPSOID SURFACE

An ellipsoid surface presents the elevation data, which causes the SWPs to diverge from the hilltop. The [39]'s formula is more hillslope than [23], but the theoretical SCAs are the same. The formula of the Zhou's surface [23] is

$$z = c \cdot \left(1 - \frac{x^2}{a^2} - \frac{y^2}{b^2}\right)^{\frac{1}{2}}. \tag{25}$$

The formula of the Qin's surface [39] is

$$z = \frac{c}{2} \cdot \left(1 + \cos \pi \sqrt{\frac{x^2}{a^2} + \frac{y^2}{b^2}}\right). \tag{26}$$

At any observed point, both surfaces have the same direction of the surface water path with the formula

$$y = kx^{\frac{a^2}{b^2}}, \tag{27}$$

and they have the same values of the specific catchment area with the formula

$$\text{SCA} = \frac{\sqrt{a^4y^2 + b^4x^2}}{a^2 + b^2}, \tag{28}$$

where $a$, $b$, $c$ and $k$ are constants.

#### 2) INVERTED ELLIPSOID

An inverted ellipsoid surface presents the elevation data, which causes the SWPs to converge into the pit. The [39]'s formula is more hillslope than [23], but the theoretical SCAs are the same. The formula of the Zhou's surface [23] is

$$z = -c \cdot \left(1 - \frac{x^2}{a^2} - \frac{y^2}{b^2}\right)^{\frac{1}{2}}. \tag{29}$$

The formula of the Qin's surface [39] is

$$z = -\frac{c}{2} \cdot \left(1 + \cos \pi \sqrt{\frac{x^2}{a^2} + \frac{y^2}{b^2}}\right), \tag{30}$$

At any observed point, both surfaces have the same surface water path, and they have the same values of the specific catchment area with the formula

$$\text{SCA} = \begin{cases} \left(\left(\frac{x_u}{x}\right)^{m+1} - 1\right) \frac{\sqrt{a^4y^2+b^4x^2}}{a^2+b^2} & \text{if } x \neq 0, \\ \left(\left(\frac{y_u}{y}\right)^{m+1} - 1\right) \frac{\sqrt{a^4y^2+b^4x^2}}{a^2+b^2} & \text{if } x = 0, \end{cases} \tag{31}$$

where $a$, $b$ and $c$ are constants.

#### 3) INCLINED PLANE

An inclined surface presents the elevation data, which causes the SWPs to be parallel with the direction from the hilltop to the bottom. The formula of the Zhou's surface [23] is

$$z = ax + by + c, \quad \text{if} -A < x, y < A. \tag{32}$$

At any observed point, the inclined plane surface has the direction of the SWPs with the formula

$$y = \frac{b}{a}x + k, \tag{33}$$

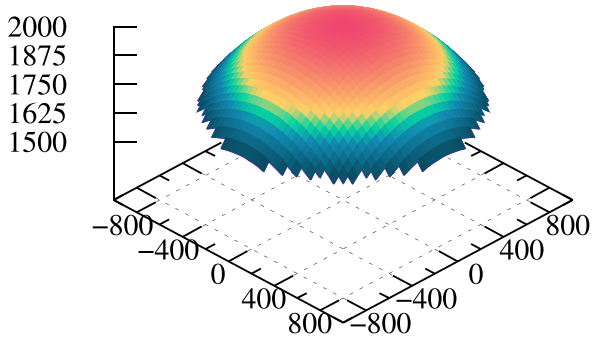


(a) Zhou's Formula

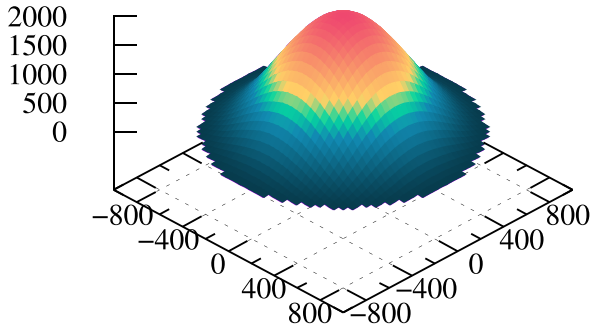


(b) Qin's Formula

**FIGURE 11.** Ellipsoid surface.

and it has the value of the SCA with the formula

$$\text{SCA} = \left(\frac{A - x}{a}\right)\sqrt{a^2 + b^2}, \tag{34}$$

where the flow path intersects with $x = A$, or another formula, that is

$$\text{SCA} = \left(\frac{A - y}{a}\right)\sqrt{a^2 + b^2}, \tag{35}$$

where flow path intersects with $y = A$, and $a$, $b$ and $c$ are constants.

### B. ESTIMATED SCA OVER ELLIPSOID

This section demonstrates that the proposed algorithm can estimate the SCAs over an ellipsoid more accurately than the existing algorithms. The demonstration comprised four main steps: i) the creation of elevation data, ii) the generation of the contour lines, iii) the delineation of the extracted SWPs, and iv) the estimation of the SCAs.

In the creation of elevation data, this work uses the ellipsoid formulas of (25) and (26) to calculate the elevation data of the Zhou's surface and the Qin's surface, respectively. For a fair comparison, we refer to the constant values in Table 1 of [10] to substitute these constants into the formulas of (25) and (26), where the constants $a$, $b$, and $c$ equal 1600, 1600, and 2000, respectively. Then, we plot the elevation data in Fig.11. Note that there is a clear distinction between the two surfaces' elevations. The Qin's surface is steeper than Zhou's surface.

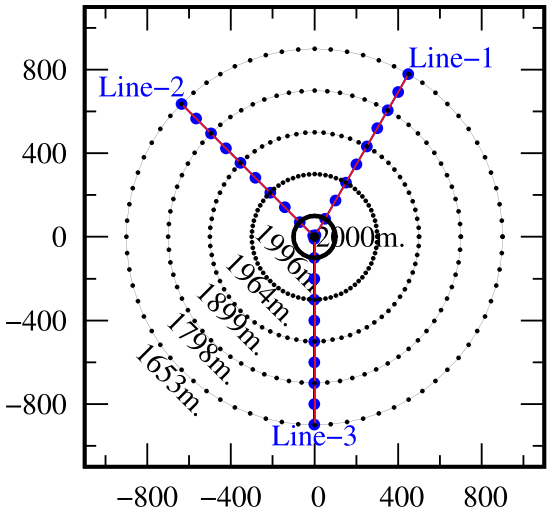


(a) Surface water paths over the Zhou's surface

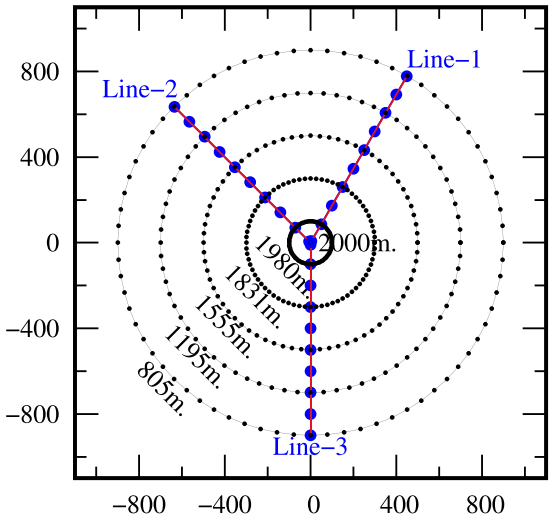


(b) Surface water paths over the Qin's surface

**FIGURE 12.** SWPs over Ellipsoids: Positions of sampled points along contour lines and positions of the extracted SWPs, including Line-1, Line-2 and Line-3. The sampled points are plotted by the black points. The theoretical and extracted SWPs are plotted by the red lines and the blue circle points.

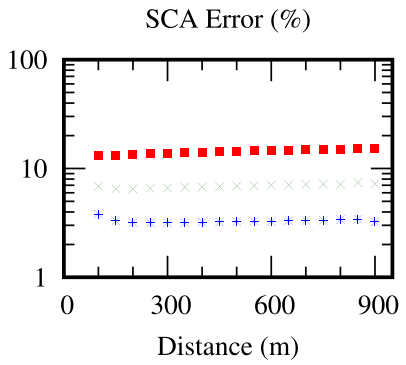


(a) SCA errors along the extracted SWP Line-1.

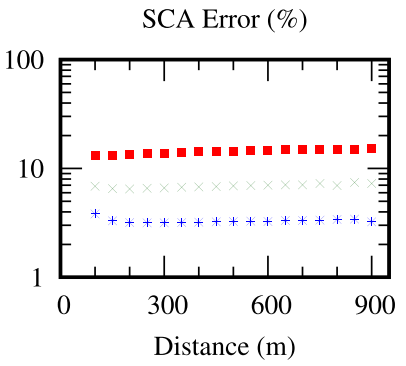


(b) SCA errors along the extracted SWP Line-2.

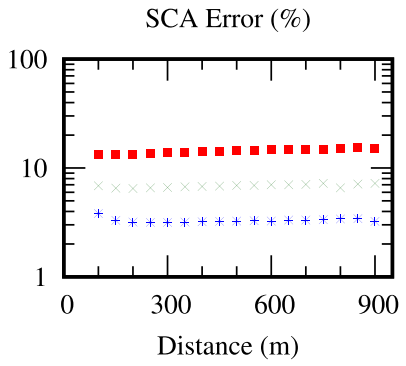


(c) SCA errors along the extracted SWP Line-3.

**FIGURE 13.** SCA error over Zhou's ellipsoid: The SCA errors at a sampling rate of every 5, 2.5 and 1.25 degrees along a contour line are plotted by the red square, green cross and blue star points, respectively.

To generate the contour lines, this work uses the same shape of contour lines over Zhou's surface and Qin's surface and plots them in Fig. 12. The positions of the six contours are on the circumferences of circles having a radius of 900, 700, 500, 300, 100, and 10 meters, respectively. The elevation levels of Zhou's contours are 2000, 1996, 1964, 1899, 1798, and 1653 meters, whereas Qin's contours are 2000, 1980, 1831, 1555, 1195, and 805 meters. To adjust the resolution of the elevation data along the contour, the number of discrete points along a contour depends on the sampling rate, which is chosen to be every 5, 2.5, or 1.25 degrees.

To delineate the SWPs over the ellipsoid, this work determines the positions of the SWPs with the contour-based algorithm [1]. The obtained SWP positions will be used to estimate SCA in the next step. We locate three observed points along the 900-meter contour and trace the SWPs in the reverse direction, starting from the observed points to the upper contour. Fig. 12a presents the three extracted SWPs over Zhou's surface in different azimuth angles, namely 60, 135, and 270 degrees, where the extracted SWPs are labeled by "Line-1", "Line-2", and "Line-3", respectively. Similarly, Fig. 12b presented the extracted SWPs over Qin's surface. The red lines in both figures present the theoretical SWPs. The differences between the obtained SWPs and the theoretical SWPs are not discernible for both Zhou's and Qin's surfaces. Therefore, the algorithm of [1] can

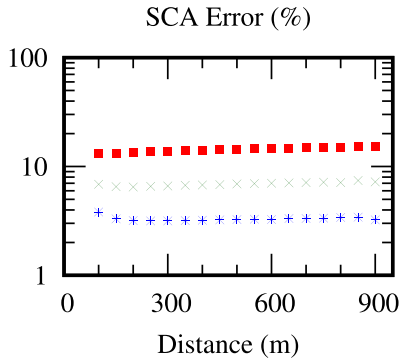


(a) SCA errors along the extracted SWP Line-1.

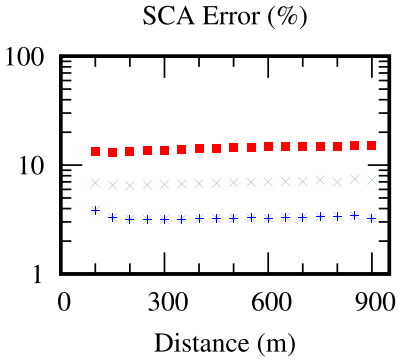


(b) SCA errors along the extracted SWP Line-2.

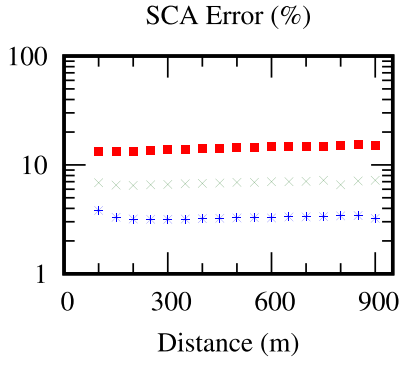


(c) SCA errors along the extracted SWP Line-3.

**FIGURE 14.** SCA error over Qin's ellipsoid: The SCA errors at a sampling rate of every 5, 2.5 and 1.25 degrees along a contour line are plotted by the red square, green cross and blue star points, respectively.

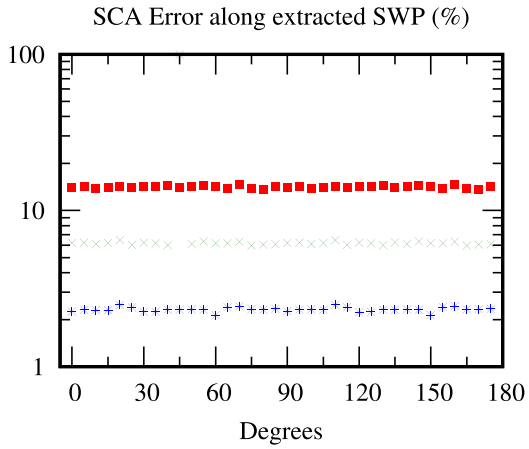


**FIGURE 15.** SCA error over Zhou's ellipsoid: The observed points are along the contour of the 900-meter radius. The SCA errors at a sampling rate of every 5, 2.5 and 1.25 degrees along a contour line are plotted by the red square, green cross and blue star points, respectively.

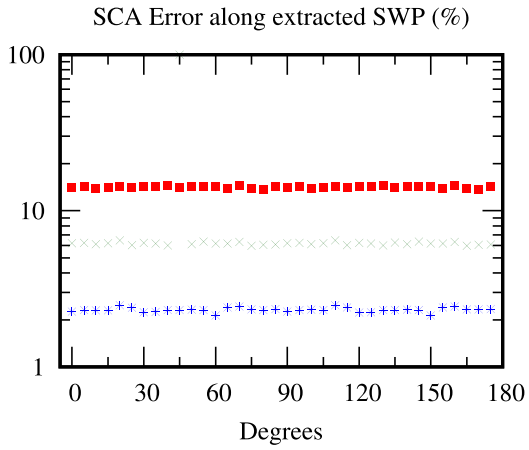


**FIGURE 16.** SCA error over Qin's ellipsoid: The observed points are along the contour of the 900-meter radius. The SCA errors at a sampling rate of every 5, 2.5 and 1.25 degrees along a contour line are plotted by the red square, green cross and blue star points, respectively.

be effectively applied to ellipsoid surfaces with various hillslopes.

To estimate the SCAs, this work uses the positions of the extracted SWPs to calculate the SCAs with Algorithm 1. Then, we measure the error percentage of the estimated SCA with the formula

$$E(\%) = \frac{|\mathrm{SCA}_{Est} - \mathrm{SCA}_{Exact}|}{\mathrm{SCA}_{Exact}} \times 100, \qquad (36)$$

where $\mathrm{SCA}_{Exact}$ is the theoretical SCA, and $\mathrm{SCA}_{Est}$ is the estimated SCA.

In Zhou's surface, Fig. 13 presents the SCA error $E(\%)$ versus the distance from the upper contour to the observed points. The SCA errors $E(\%)$ at the points along the SWP Line-1 are obtained from (36) and plotted in Fig. 13a. Similarly, the SCA errors at the points along the SWPs Line-2 and Line-3 are plotted in Fig. 13b and 13c, respectively. Next, Fig. 14 presents the SCA error $E(\%)$ over Qin'surface. The SCA errors of Zhou's and Qin's surfaces are hardly different. Only at a sampling rate of every 5 degrees (red square markers), the average error is less than 15% for both surfaces. At a higher sampling rate, namely every 2.5 and 1.25 degrees, the SCA errors significantly decrease. For example, in Fig. 13a, at a radius of 900 meters, E(%) along the SWP Line-1 decreases from 14.2807 to 3.1363. The same trend can be observed from Qin's surface in Fig. 14a.

The proposed algorithm performs well not only at various distances but also at various directions. Fig. 15 presents the SCA error $E(\%)$ over Zhou's surface versus the azimuth angle. The SCA errors over Qin's surface are plotted in

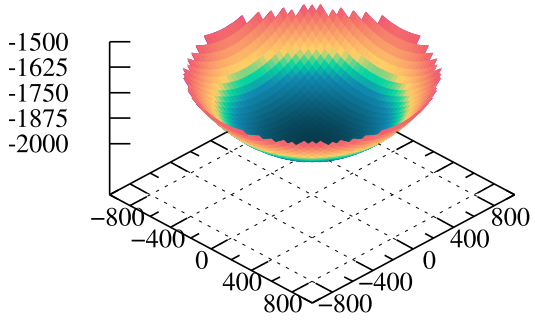


(a) Zhou's Formula

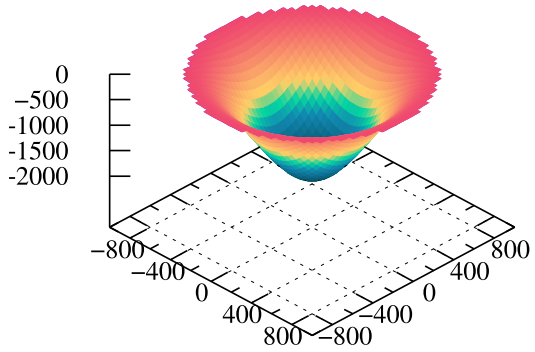


(b) Qin's Formula

**FIGURE 17.** Inverted Ellipsoid Surface.

Fig. 16. The SCA errors of Zhou's and Qin's surfaces are hardly different. Only at a sampling rate of every 5 degrees (red square markers), the average error is less than 15% for both surfaces. At a higher sampling rate, namely every 2.5 and 1.25 degrees, the SCA errors significantly decrease. The same trend can be observed from the Qin's surface in Fig. 16.

### C. ESTIMATED SCA OVER INVERTED ELLIPSOID

This section demonstrates that the proposed algorithm can estimate the SCAs over an inverted ellipsoid more accurately than the existing algorithms. Similar to Section III-B, the demonstration comprised four main steps: i) the creation of elevation data, ii) the generation of the contour lines, iii) the delineation of the extracted SWPs, and iv) the estimation of the SCAs.

To create the elevation data, this work uses the inverted ellipsoid formulas of (29) and (30) to calculate the elevation data of Zhou's and Qin's surfaces, respectively. For a fair comparison, we refer to the constant values in Table 1 of [10] to substitute these constants into the formulas of (29) and (30), where the constants $a$, $b$, and $c$ equal 1600, 1600, and 2000, respectively. Then, we plot the elevation data in Fig. 17. Note that there is a clear distinction between the two surfaces' elevations. The Qin's surface is steeper than Zhou's surface.

To generate the contour lines, this work uses the same shape of contour lines over Zhou's surface and Qin's surface

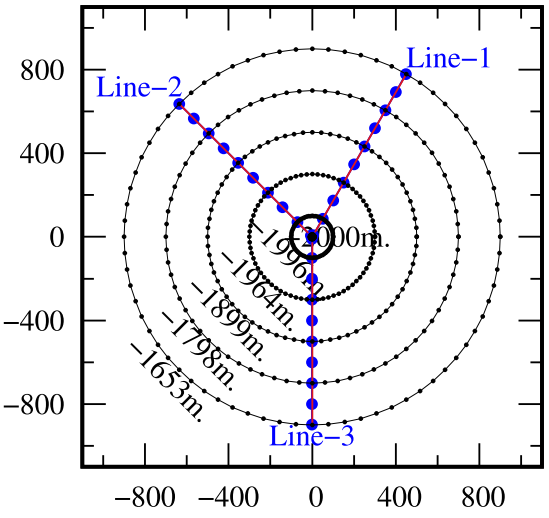


(a) Surface water paths over the Zhou's surface

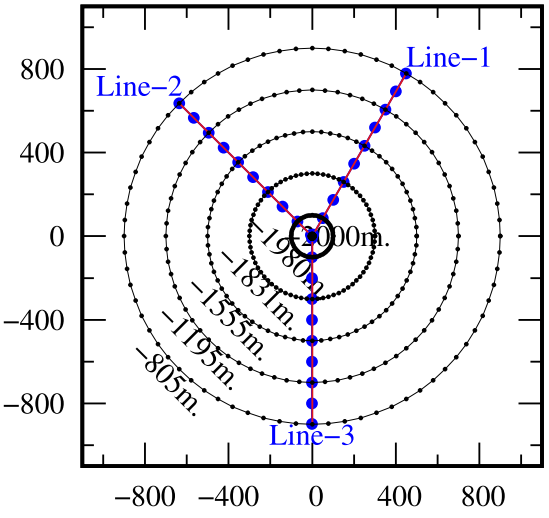


(b) Surface water paths over the Qin's surface

**FIGURE 18.** SWPs over inverted ellipsoids: Positions of sampled points along contour lines and positions of the extracted SWPs including Line-1, Line-2 and Line-3. The sampled points are plotted by the black points. The theoretical and extracted SWPs are plotted by the red lines and the blue circle points.

and plots them in Fig. 18. The positions of the six contours are on the circumferences of circles having a radius of 10, 100, 300, 500, 700, and 900 meters, respectively. The elevation levels of Zhou's contours are −2000, −1996, −1964, −1899, −1798, and −1653 meters, whereas Qin's contours are −2000, −1980, −1831, −1555, −1195, and −805 meters. To adjust the resolution of the elevation data along the contour, the number of discrete points along a contour depends on the sampling rate, which is chosen to be every 5, 2.5, and 1.25 degrees.

To delineate the SWPs over the inverted ellipsoid, this work determines the positions of the SWPs with the contour-based algorithm [1]. The obtained SWP positions will be used to estimate SCA in the next step. We locate three observed

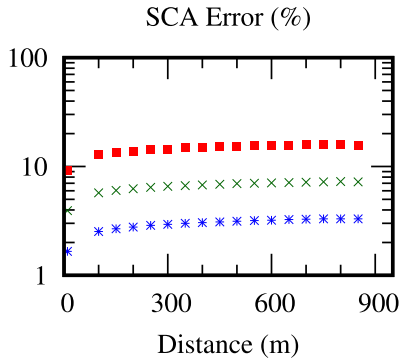


(a) SCA errors along the extracted SWP Line-1.

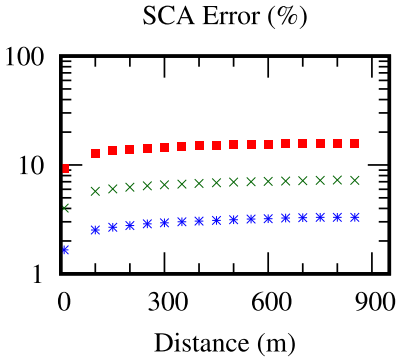


(b) SCA errors along the extracted SWP Line-2.

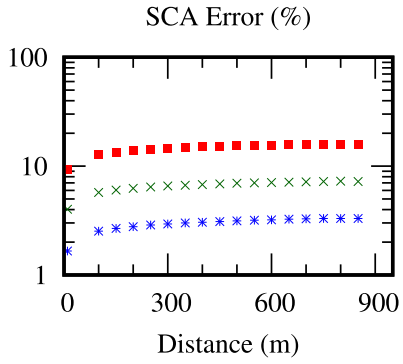


(c) SCA errors along the extracted SWP Line-3.

**FIGURE 19.** SCA errors over Zhou's inverted ellipsoid: The SCA errors at a sampling rate of every 5, 2.5 and 1.25 degrees along a contour line are plotted by the red square, green cross and blue star points, respectively.

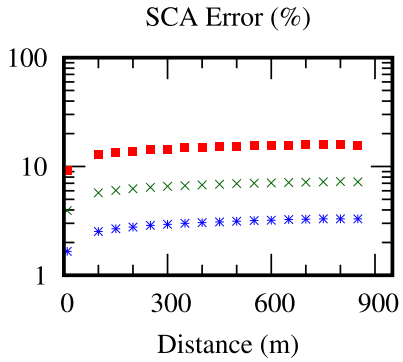


(a) SCA errors along the extracted SWP Line-1.

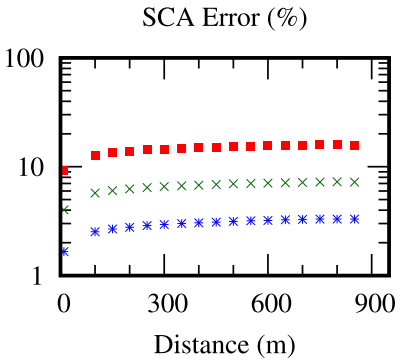


(b) SCA errors along the extracted SWP Line-2.

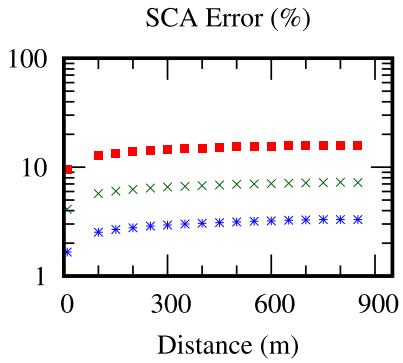


(c) SCA errors along the extracted SWP Line-3.

**FIGURE 20.** SCA errors over Qin's inverted ellipsoid: The SCA errors at a sampling rate of every 5, 2.5 and 1.25 degrees along a contour line are plotted by the red square, green cross and blue star points, respectively.

points along the 10-meter contour and trace the SWPs in the reverse direction, starting from the observed point to the upper contour. Fig. 18a presents the three extracted SWPs over Zhou's surface in different azimuth angles, namely 60, 135, and 270 degrees, where the extracted SWPs are labeled by "Line-1", "Line-2", and "Line-3", respectively. Similarly, Fig. 18b presents the extracted SWPs over Qin's surface. The red lines in both figures present the theoretical SWPs. The differences between the obtained SWPs and the theoretical SWPs are not discernible for both Zhou's and Qin's surfaces. Therefore, the algorithm of [1] can be effectively applied to inverted ellipsoid surfaces with various hillslopes.

To estimate the SCAs, this work uses the positions of the extracted SWPs to calculate the SCAs with Algorithm 1. Then, we measure the error percentage of the estimated SCA with the formula of (36).

In Zhou's surface, Fig.19 presents the SCA error $E(\%)$ versus the distance from the upper contour to the observed points. The SCA errors $E(\%)$ at the points along the SWP Line-1 are obtained from (36) and plotted in Fig. 19a. Similarly, the SCA errors at the points along the SWP Line-2 and Line-3 are plotted in Fig. 19b and 19c, respectively. Next, Fig. 20 presents the SCA errors $E(\%)$ over Qin'surface. The SCA errors of Zhou's and Qin's surfaces are hardly

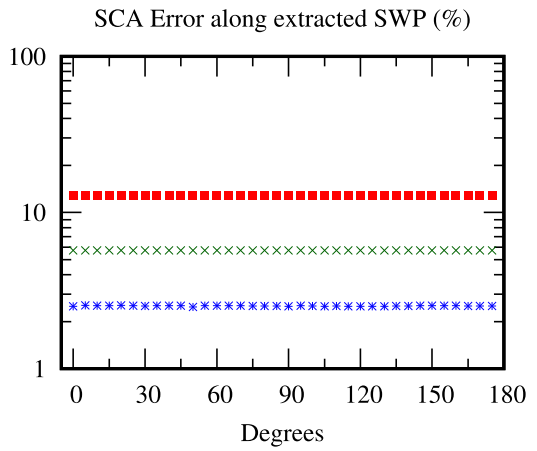


**FIGURE 21.** SCA errors over Zhou's inverted ellipsoid: The observed points are along the contour with a radius of 10-meter. The SCA errors at a sampling rate of every 5, 2.5 and 1.25 degrees along a contour line are plotted by the red square, green cross and blue star points, respectively.

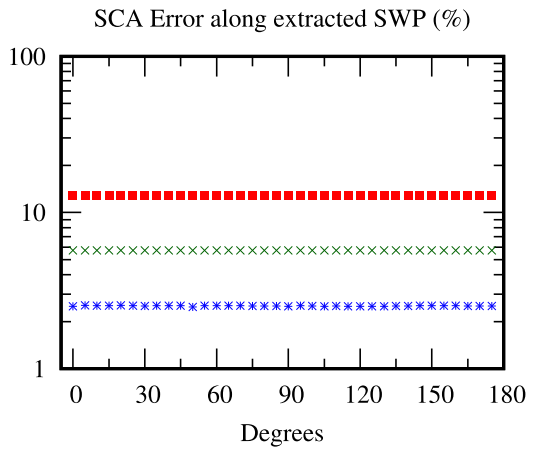


**FIGURE 22.** SCA errors over Qin's inverted ellipsoid: The observed points are along the contour with a radius of 10-meter. The SCA errors at a sampling rate of every 5, 2.5 and 1.25 degrees along a contour line are plotted by the red square, green cross and blue star points, respectively.

different. Only at a sampling rate of every 5 degrees (red square markers), the average error is less than 13% for both surfaces. At a higher sampling rate, namely every 2.5 and 1.25 degrees, the SCA errors significantly decrease. For example, in Fig. 19, at a radius of 100 meters, E(%) along the SWP Line-1 decreases from 12.9749 to 2.6582. The same trend can be observed from Qin's surfaces in Fig. 20.

The proposed algorithm performs well not only at various distances but also at various directions. Fig. 21 presents the SCA error $E(\%)$ over Zhou's surface versus the azimuth angle. The SCA error $E(\%)$ over Qin's surface are plotted in Fig. 22. The SCA errors of Zhou's and Qin's surfaces are hardly different. Only at a sampling rate of every 5 degrees (red square markers), the average error is less than 13% for both surfaces. At a higher sampling rate, namely every 2.5 and 1.25 degrees, the SCA errors significantly decrease. The same trend can be observed from the Qin's surface in Fig. 22.

### D. ESTIMATED SCA OVER INCLINED PLANE

This section demonstrates that the proposed algorithm can estimate the SCAs over an inclined plane more accurately than the existing algorithms. Similar to Section III-B, the demonstration comprised four main steps: i) the creation of elevation data, ii) the generation of the contour lines, iii) the delineation of the extracted SWPs, and iv) the estimation of the SCAs.

To create the elevation data, this work uses the inclined plane formulas of (32) to calculate the elevation data of Zhou's surface. Note that there is no inclined plane in case of Qin's surface. For a fair comparison, we refer to the constant values in Table 1 of [10] to substitute these constants into the formula of (32), where the constants $a$, $b$, $c$ and $A$ equal 2, 1.5, 3250 and 900, respectively. Then, we plot the elevation data in Fig.23.

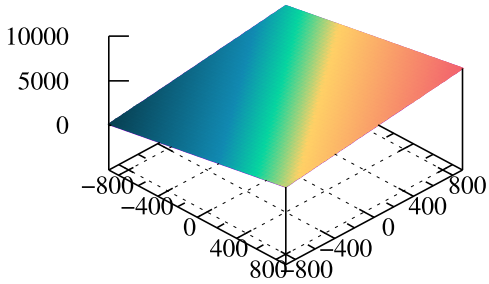


**FIGURE 23.** Incline plane by Zhou [23].

To generate the contour lines, this work uses the square shape of a contour line over Zhou's surface and plots it in Fig. 24. Along the contour, the four corner points have different elevation levels, namely 100, 2800, 3700, and 6400 meters, respectively.

To delineate the SWPs over the inclined plane, this work determines the positions of the SWPs with the contour-based algorithm [1]. The obtained SWP positions will be used to estimate SCA in the next step. We locate three observed points at the coordinates of (−900,200), (−250,−900), and (−850,−900) and trace the SWPs in the reverse direction, starting from the observed point to upper contour. Fig. 24 presents the three extracted SWPs, namely the SWP "Line-1", "Line-2", and "Line-3". The red lines presented the theoretical SWPs. The differences between the obtained SWPs and the theoretical SWPs are not discernible. Therefore, the algorithm of [1] can be effectively applied to inclined plane.

To estimate the SCAs, this work uses the positions of the extracted SWPs to calculate the SCAs with Algorithm 1. Then, we measure the error percentage of the estimated SCA with the formula of (36).

Fig. 25 presents the SCA error $E(\%)$ versus the distance from the upper contour to the observed points. The SCA errors $E(\%)$ at the points along the SWP Line-1 are obtained

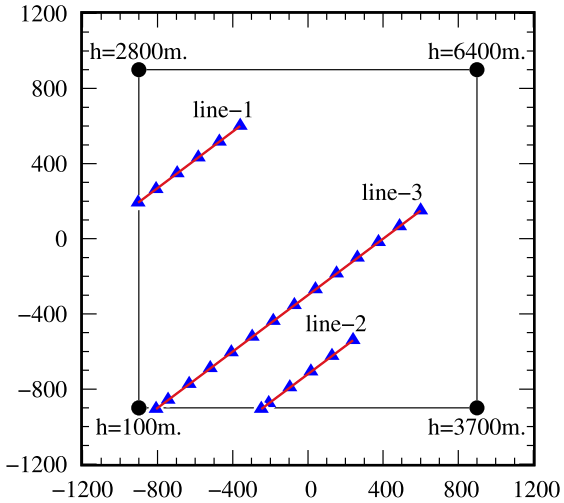


**FIGURE 24.** Positions of sampled points along contour lines and positions of the extracted SWPs including Line-1, Line-2 and Line-3. The sampled points are plotted by the black points. The theoretical and extracted SWPs are plotted by the red lines and the blue triangular points, respectively.

**TABLE 1.** Ellipsoid: Comparison of average SCA error (%).

| Algorithms | Resolution | | |
|---|---|---|---|
| | Low | Med | High |
| Proposed: | | | |
| Number of sampled points along contour line | 72 | 144 | 288 |
| Lengths of intervals along contour line (m) | 78.5 | 39.25 | 19.625 |
| Error (%) | 14.19 | 6.16 | 2.32 |
| Others: | | | |
| Number of cells | 10x10 | 60x60 | 120x120 |
| cell size (m) | 90 | 15 | 7.5 |
| D8 | 35.0 | 43.5 | 44.4 |
| Rho-8 | 37.5 | 41.7 | 42.8 |
| D8-LTD | 35.3 | 42.1 | 42.8 |
| FDFM | 26.8 | 31.9 | 32.8 |
| FMD-md | 27.3 | 42.4 | 43.3 |
| D∞ | 36.4 | 43.1 | 44.1 |

from (36) and are plotted in Fig. 25. The same trend can be observed from the SWP Line-2 and Line-3.

### E. COMPARISON TO OTHER ALGORITHMS

This section shows that when the DEM resolution is higher, the proposed physically-based algorithm can increase the accuracy of the catchment estimation while the existing algorithms cannot. The averaged SCA errors from the previous subsection are compared with the averaged SCA errors from [10]. The referred errors are the SCA errors of the popular grid-based algorithms, namely D8, Rho-8, D8-LTD, FDFM, FMD-MD, and D∞.

Table 1 shows the averaged SCA errors in the case of an ellipsoid surface. The proposed algorithm calculates the average SCA errors from three different resolutions of the elevation data. The previous subsection shows the results with

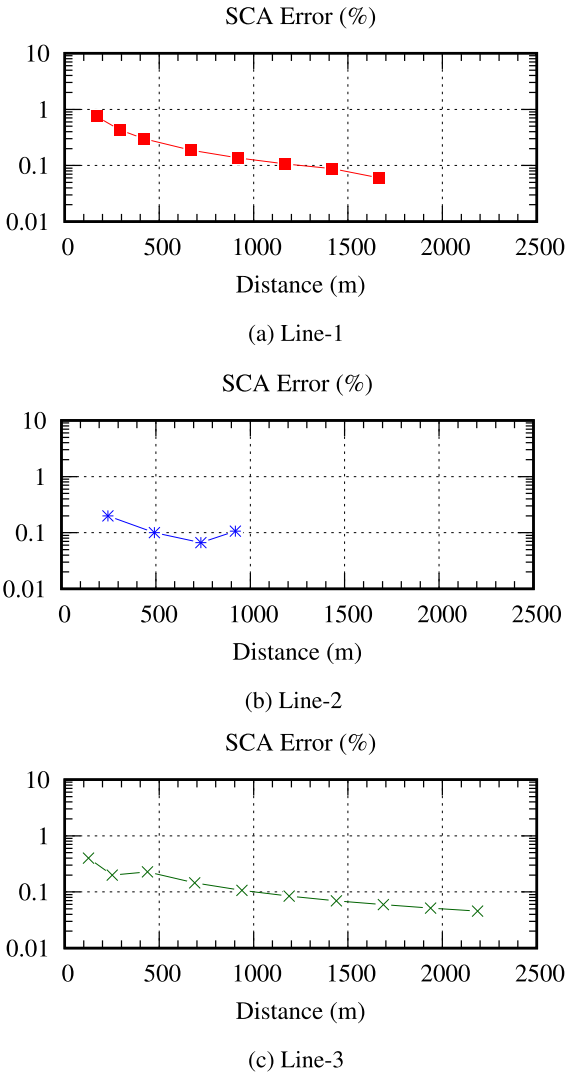


**FIGURE 25.** SCA errors over inclined plane.

the low resolution in detail, and this subsection illustrates the trend of the results when increasing the resolutions. The proposed algorithm can improve the accuracy of the average SCA by increasing the sampling rates of the elevation data along a contour with a radius of 900 meters. In a contour-based algorithm, increasing resolution makes the interval between sampled points along the contour line shorter. In Section III-B, when we sampled the contour-based data at every 5, 2.5, and 1.25 degrees along a circle, we obtained the number of contour intervals $N_{\text{Points}}$ of 72, 144, and 288, respectively. The interval length along a contour depends on the radius of the sampled contour line, and interval length equals $\frac{2\pi R}{N_{\text{Points}}}$. For example, when estimating the catchment and locating the observed point along a 900-meter contour, the interval length is 78.5, 39.25, and 19.625 meters. For a fair comparison, we set the length of each interval according to the grid-based DEM resolutions, which are used to assess the errors of the existing algorithms in [10]. The grid-based resolutions are determined by the image cell sizes: 90.0, 15.0,

**TABLE 2.** Inverted Ellipsoid: Comparison of average SCA error (%).

| Algorithms | Resolution | | |
|---|---|---|---|
| | Low | Med | High |
| Proposed: | | | |
| Number of sampled points along contour line | 72 | 144 | 288 |
| Lengths of intervals along contour line (m) | 78.5 | 39.25 | 19.625 |
| Error (%) | 12.97 | 5.85 | 2.65 |
| Others: | | | |
| Number of cells | 10x10 | 60x60 | 120x120 |
| cell size (m) | 90 | 15 | 7.5 |
| D8 | 49.3 | 46.2 | 45.1 |
| Rho-8 | 50.9 | 46.2 | 45.1 |
| D8-LTD | 63.8 | 47.6 | 46.9 |
| FDFM | 77.8 | 75.2 | 73.5 |
| FMD-md | 54.5 | 47.3 | 46.9 |
| D$\infty$ | 49.7 | 46.2 | 45.1 |

**TABLE 3.** Inclined plane: Comparison of average SCA error (%).

| Algorithms | Resolution | | |
|---|---|---|---|
| | Low | Med | High |
| Proposed: | | | |
| Number of sampled points along contour line | 4 | - | - |
| Lengths of intervals along contour line (m) | 1800 | - | - |
| Error (%) | 0.184 | - | - |
| Others: | | | |
| Number of cells | 10x10 | 60x60 | 90x90 |
| cell size (m) | 90 | 15 | 10 |
| D8 | 42.3 | 47.4 | 47.5 |
| Rho-8 | 40.4 | 41.2 | 41.9 |
| D8-LTD | 36.4 | 41.0 | 41.2 |
| FDFM | 17.0 | 20.1 | 20.6 |
| FMD-md | 38.6 | 43.6 | 44.1 |
| D$\infty$ | 37.8 | 42.9 | 43.4 |

and 7.5 meters. At low resolution, the proposed algorithm gives the average SCA error equal to 14.19%, whereas the FDFM algorithm is 26.8%, which is the best. When increasing the resolution, the proposed algorithm reduces the average SCA error to 6.16 and 2.32, respectively, but the other algorithms show no improvement at all.

Table 2 shows the averaged SCA errors in the case of an inverted ellipsoid surface. Similar to the ellipsoid case, the proposed algorithm improves the average SCA errors by increasing the elevation resolution. At low resolution, the proposed algorithm gives an average SCA error of 12.97%, whereas all other algorithms' average errors are greater or equal to 49.3%. When increasing the resolution, the proposed algorithm reduces the average SCA error to 5.85 and 2.65, respectively, while all other algorithms' average errors are greater than or equal to 45.1%.

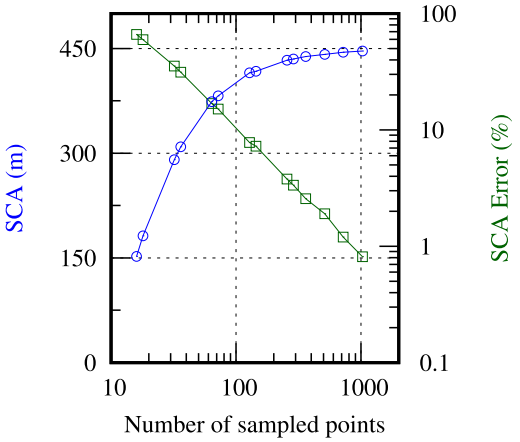


**FIGURE 26.** Ellipsoid: SCA error versus NQ at the observed contour. The radius of the observed contour line has a length of $R = 900$ meters.

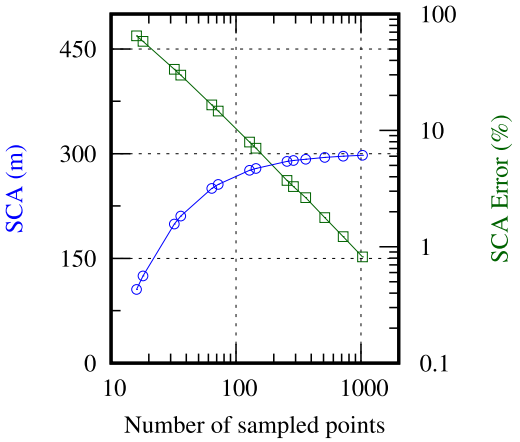


**FIGURE 27.** Ellipsoid: SCA error versus NQ at the observed contour. The radius of the observed contour line has a length of $R = 600$ meters.

Table 3 shows the averaged SCA errors in the case of an inclined plane. Even at the lowest resolution of elevation data, the proposed algorithm gives an average SCA error of 0.184%. Regardless of the resolution, only four elevation data are enough to represent the entire inclined plane. In contrast, all other algorithms' average errors are greater or equal to 17.0%.

### F. IMPROVED ACCURACY WITH HIGHER RESOLUTION DEM

In the future, high-resolution DEMs will be available. Unfortunately, higher resolutions do not lower the average SCA errors of existing algorithms [10], which inspired us to develop the proposed algorithm. From the previous section, it is obvious that the accuracy of the proposed algorithm is higher than that of existing algorithms, especially when the resolution becomes higher. In this section, we keep increasing the resolution to observe the accuracy improvement trend of the proposed algorithm.

Fig.26 to Fig.28 and Fig.29 to Fig.31 present the average SCA errors as a function of resolution on the ellipsoid and

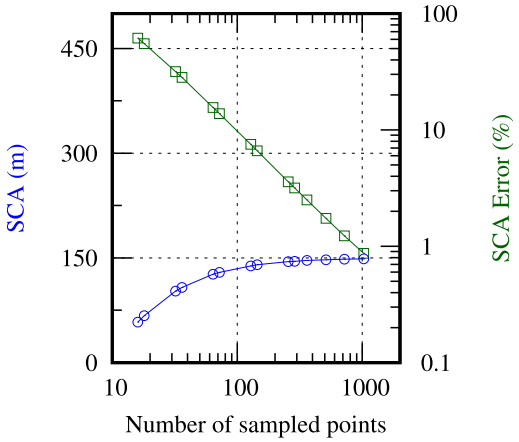


**FIGURE 28.** Ellipsoid: SCA error versus NQ at the observed contour. The radius of the observed contour line has a length of $R = 300$ meters.

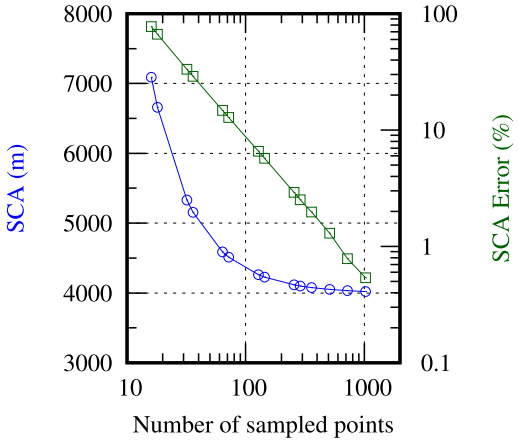


**FIGURE 29.** Inverted ellipsoid: SCA error versus NQ at the observed contour. The radius of the observed contour line has a length of $R = 100$ meters.

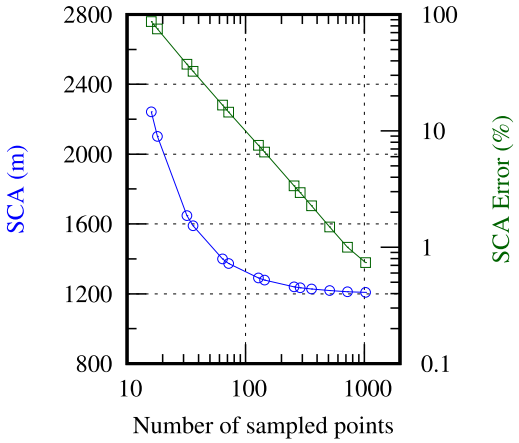


**FIGURE 30.** Inverted ellipsoid: SCA error versus NQ at the observed contour. The radius of the observed contour line has a length of $R = 300$ meters.

inverted ellipsoid surfaces, respectively. The average SCA errors are the obtained results from the same assessment process in the previous section. Note that the resolutions are

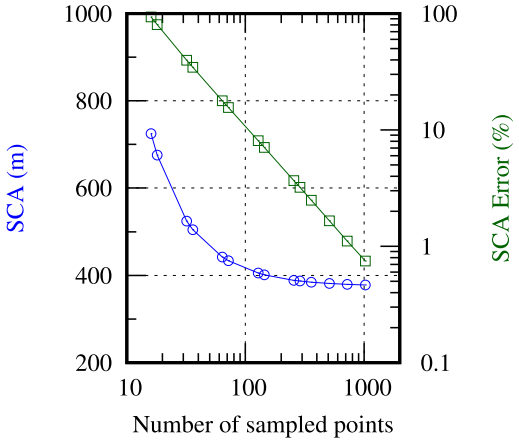


**FIGURE 31.** Inverted ellipsoid: SCA error versus NQ at the observed contour. The radius of the observed contour line has a length of $R = 600$ meters.

contour-based. The contour-based resolution is the interval of the sampled points along the contour line. Here, the number of the sampled points along the contour line equals $2^n$ where $n = 5, 6, \ldots, 10$. The interval length along a contour depends on the radius of the sampled contour line, and interval length equals $\frac{2\pi R}{N_{\text{Points}}}$. For example, when estimating the catchment and locating the observed point along a 900-meter contour, the interval length is between 176.78 and 5.523 meters.

In ellipsoid, Fig.26 plots the values of the estimated SCAs at any observed point along the contour with a radius of 900 meters with the blue circle points. The same figure plots the average SCA errors with green rectangular points. By keep increasing the resolution, the estimated SCA approaches a theoretical value of 450 meters. In other words, the average SCA error approaches zero. For example, when increasing the sampled points along a contour from $n = 5$ to $n = 10$, the length of the contour interval decreases from 176.78 to 5.523 meters, and the average SCA error decreases from 70.0 to 0.819%. Similar to Fig.26, Fig.27 presents the average SCA error at any observed point along the contour with a radius of 600 meters with the blue circle points. The average SCA error decreases from 70.0 to 0.827%, increasing from $n = 5$ to $n = 10$ or decreasing the contour interval length from 117.86 to 3.68 meters. Also, at any observed point along the contour with a radius of 300 meters, in Fig.28, the average SCA error decreases from 70.0 to 0.877%, when increasing $n = 5$ and $n = 10$, or decreasing the contour interval length from 58.93 to 1.84 meters. Therefore, the proposed algorithm can give the average SCA error less than 5% if the number of sampled points is more than 200.

In an inverted ellipsoid, Fig.29 plots the values of the estimated SCAs at any observed points along the contour with a radius of 100 meters with the blue circle points. The same figure plots the average SCA errors with green rectangular points. By keep increasing the resolution, the estimated SCA approaches a theoretical value of 4000 meters. In other words, the average SCA error approaches zero. For example, when

increasing the sampled points along a contour form $n = 5$ to $n = 10$, the length of the contour interval decrease from 19.64 to 0.61 meters, and the average SCA error decreases from 80 to 0.746%. Similar to Fig.29, Fig.30 presents the average SCA error at any observed point along the contour with a radius of 300 meters with the blue circle points. The average SCA error decreases from 90 to 0.739%, increasing from $n = 5$ to $n = 10$ or decreasing the contour interval length from 58.93 to 1.84 meters. Also, at any observed point along the contour with a radius of 600 meters, in Fig.31, the average SCA error decreases from 95 to 0.746%, when increasing from $n = 5$ to $n = 10$ or decreasing the contour interval length from 117.86 to 3.68 meters. Therefore, the proposed algorithm can give the average SCA error less than 5% if the number of sampled points is more than 200.

### G. DISCUSSION

This section discusses two main issues related to the proposed algorithm for catchment estimation from digital elevation models (DEM) based on contour lines. The first issue is the catchment estimation and sub-watershed partition delineation using a physically-based algorithm and synthetic surface validation. The second issue is the implementation of the proposed algorithm for analyzing catchments over natural terrains.

#### 1) VALIDATION THROUGH SYNTHETIC SURFACES

The experiments conclude that the proposed algorithm can increase the catchment estimation accuracy with the DEM-based data having a future resolution, where the existing grid-based algorithms cannot. The key feature of the proposed algorithm is the physically-based concept and converting the semi-analytical solution of the differential equation into the numerical solution with the BEM. Furthermore, the experiments point out that the BEM-based solution gives more accurate numerical results, namely the slope and its gradients when increasing the precision of the information along the contour lines. Then, the proposed algorithm can control the error of the estimated catchment and the mistake of the delineated SWPs.

This work gains the advantages of a physically-based algorithm to significantly enhance the catchment estimation and the SWP delineation from the DEM images. In estimating the catchment, the proposed algorithm uses two main physically-based values. First, the algorithm uses the positions of the extracted SWPs from [1]'s algorithm, which delineates the SWPs with the numerical solution of Laplace's equation. Second, the algorithm uses the values of the hillslope from the same numerical solution for calculating the size of the catchment area element along the positions of the extracted SWPs. Moreover, the algorithm uses the principal features of the numerical solution based on BEM, which can discretize the problem domain along the contour lines instead of the areas surrounding the contour lines. Thus, the problem domain is in one variable instead of two, and the computation resources are less demanding. Accordingly, the physically-based algorithm of [1] can improve the accuracy of the extracted SWP positions from DEM image, and the proposed algorithm, which is the physically-based algorithm, can significantly reduce the SCA estimation error with higher resolution DEM.

This work uses the method in [10] to measure the SCA error, compared with the theoretical SCA to validate the proposed algorithm. The validation uses the standard synthetic surfaces, derived from [23], namely ellipsoid, inverted ellipsoid, and inclined plane, where theoretical SCAs exist. We also use the synthetic surfaces in [39], where the hillslopes are steeper and more realistic than those in [23]. The results show that even at low resolution the average SCA error $E(\%)$ of the proposed algorithm is less than those of all grid-based algorithms at any resolution.

When a super-resolution DEM image is available, the proposed algorithm can exploit the higher resolution to improve the catchment estimation accuracy, whereas the existing algorithms cannot. In the experiment, the higher resolution is introduced by decreasing the interval of the sampled points along the contour line from 12.5 to 0.88 meters. As a result, the average SCA errors are reduced from 15% to 0.8%. Very low SCA estimation error will help hydrologists to forecast floods more precisely.

#### 2) IMPLEMENTATION FOR A NATURAL TERRAIN

When analyzing the catchment over a natural landscape comprising various surfaces: hilltops, catchments, and flat planes, we must confront more complicated shapes of the contour-based data, namely high irregularity, and very long lines. But, we can treat the irregularity with a higher resolution of the DEM image. Fortunately, we will obtain the high DEM resolution because the researchers have achieved the remote-sensing and earth observation techniques. Therefore, the future contour-based DEM, which represents the primary terrain features more than the grid-based DEM, becomes more beneficial for estimating catchment. Moreover, it is an opportunity for this work because the proposed algorithm can support the higher resolution of DEM images that include various terrain features such as hilltops, sinks, and flat areas.

In the case of a large area, the contour-based data comprise the long series of the elevation at the lowland or flat region. The algorithm of [1] can remove this constraint with the physically-based concept for delineating the surface water flowing and the BEM-based solutions for Laplace's differential equation. Then, the proposed algorithm, including the algorithm of [1], can support a very long contour line when considering a large catchment area. Furthermore, enhancing the proposed algorithm for analyzing the hybrid zone, which comprises the natural and urban areas, is possible.

Although this work implies that the proposed algorithm performs the case of irregular contour lines by using higher DEM resolution, it does not mean that the proposed algorithm operates all types of irregularity, especially the significant error of the DEM image. The leading causes are the users who digitize the contours with inappropriate methods

for topographic complexity, such as interpolation, data processing and filtering, and surveying. For example, when the users generate the contours representing the elevation over a flat area in the suburban, the obtained contours often comprise poor segments, such as 8-shape and v-shape. The proposed algorithm can detect these poor contours and gives a warning. Currently, the users must correct them manually. Therefore, in case that the manual correction is not properly done, the contours with low elevations incur ambiguity that limits the performance of the proposed algorithm. To remove this problem, we need the criterion for classifying the poor contour lines and utilizing it to implement the proposed algorithm for the real DEM. The next step derives the criterion from information representing the robustness of the proposed algorithm. Also, it includes pre-processing to prepare efficient input data. The main feature of pre-processing is that it can separate the abnormal contour lines from the input data. In future work, we will implement the proposed algorithm with the criterion for a real DEM, representing the elevation over the popular case of mixing natural and residential areas.

## IV. CONCLUSION

This paper proposes a new physically based algorithm for estimating the catchment from a contour-based DEM elevation. Unlike existing methods, this algorithm utilizes a physically-based approach that calculates line integrals over the Surface Water Paths (SWPs). In the error assessment, the accuracy of the proposed algorithm is higher than those of the existing grid-based algorithms and requires less resolution of the elevation data. Furthermore, the proposed algorithm, based on the semi-analytical solution of Laplace's partial differential equation with BEM, is the only algorithm that can effectively utilize the super DEM resolutions, which will be commonly available in the future.

## APPENDIX A
## CALCULATING THE GRADIENT OF INTERPOLATED ELEVATION GRADIENT

In [1], gradient of the elevation gradients $\nabla^2 h(P)$ is the differentiation of (21), which can be expressed as

$$2\pi\nabla^2 h(P) = \int_C \vec{A}''(P,Q)\left(\nabla H(Q)\cdot\hat{n}(Q)\right)dc - \int_C \vec{B}''(P,Q)H(Q)dc, \tag{37}$$

where $Q$ represents the position of element $dc$ along the contour, and the vector functions $\vec{A}''(P,Q)$ and $\vec{B}''(P,Q)$ are the shape functions of points $P$ and $Q$, and can be expressed as

$$\vec{A}''(P,Q) = \nabla_P\left(\frac{\overrightarrow{PQ}}{\left\|\overrightarrow{PQ}\right\|^2}\right)$$

$$\vec{B}''(P,Q) = \nabla_P\left(\frac{\hat{n}(\vec{Q})}{\left\|\overrightarrow{PQ}\right\|^2}\right) - \nabla_P\left(2\frac{\overrightarrow{PQ}\cdot\hat{n}(\vec{Q})}{\left\|\overrightarrow{PQ}\right\|^4}\overrightarrow{PQ}\right). \tag{38}$$

The solution (37) is continuous, but the input DEM is discrete. Accordingly, the numerical solution was formulated in Section IV-B in [1] with boundary element method. This numerical solution can interpolate the $\nabla^2 h(P)$ by using the elevation data along the discrete contour lines. This paper rewrites the numerical solution to conform with the computer algorithm in Section II-D. For convenience, this paper describes the numerical solution in line integral form to obtain the $\nabla^2 h(P)$, which will be used to determine the next point $P_{j,k+1}$ in Section II-D. The contour lines that are the domain for line integrals are the same as the contour lines in calculating the gradient of the interpolated elevation $\nabla h(P)$ in Section II-C. For example, a contour representing discrete elevation data of $N_Q$ is the domain for line integral, as shown in Fig. 9. The contour contains discrete elevation data of $N_e$, and each segment starts from $Q_e$ to $Q_{e+1}$. As a result, the solution of $\nabla^2 h(P)$ can be determined with $N_e$ line integrals as follows.

$$2\pi\nabla^2 h(P) = \sum_{e=1}^{N_e}\int_{Q_e}^{Q_{e+1}} \vec{A}''(P,Q)\left(\nabla H(Q)\cdot\hat{n}(Q)\right)dc - \sum_{e=1}^{N_e}\int_{Q_e}^{Q_{e+1}} \vec{B}''(P,Q)H(Q)dc, \tag{39}$$

where the boundary value functions $H(Q)$ and $\nabla H(Q)$ can be solved from DEM as shown in Section III in [1].

## APPENDIX B
## STEEPEST ASCENT DETERMINATION

To find the $\theta_{\max}$, we differentiate the trace on the circle of the approximated surface, that is

$$\frac{dh}{d\theta}(r_0,\theta) = r_0\left[-h_x\sin\theta + h_y\cos\theta\right] + r_0^2\left[-h_{xx}\sin 2\theta + h_{xy}\cos 2\theta\right]. \tag{40}$$

Then, we equate the derivative to zero, that is

$$h_x\sin\theta + r_0 h_{xx}\sin 2\theta = h_y\cos\theta + r_0 h_{xy}\cos 2\theta. \tag{41}$$

To solve this equation, trigonometric identities are applied to convert the equation into a fourth-order (quartic) equation with either $\cos\theta$ term or $\sin\theta$ term. First, substituting $\sin 2\theta = 2\sin\theta\cos\theta$ and $\cos 2\theta = 2\cos^2\theta - 1$ into (41) as well as replacing $\cos\theta$ by $\nu$ and $\sin\theta$ by $\omega$, we obtain

$$(h_x + 2\,h_{xx}r_0\nu)\,\omega = h_y\nu + h_{xy}r_0\left(2\nu^2 - 1\right). \tag{42}$$

Next, since $\nu^2 + \omega^2 = 1$, $\omega$ is replaced by $\sqrt{1-\nu^2}$, that is,

$$(h_x + 2\,h_{xx}r_0\nu)\sqrt{1-\nu^2} = h_y\nu + h_{xy}r_0\left(2\nu^2 - 1\right). \tag{43}$$

Last, taking square to both sides of the equation to get rid of the square root, we obtain

$$c_4\nu^4 + c_3\nu^3 + c_2\nu^2 + c_1\nu + c_0 = 0, \tag{44}$$

where the coefficients $c_0 \ldots c_4$ equal

$$c_4 = 4\, r_0^2 \left(h_{xy}^2 + h_{xx}^2\right) \tag{45}$$

$$c_3 = 4\, r_0 \left(h_x h_{xx} + h_y h_{xy}\right) \tag{46}$$

$$c_2 = h_x^2 + h_y^2 - 4\, r_0^2 \left(h_{xx}^2 + h_{xy}^2\right) \tag{47}$$

$$c_1 = -2 r_0 \left(h_y h_{xy} + 2\, h_x h_{xx}\right) \tag{48}$$

$$c_0 = h_{xy}^2 r_0^2 - h_x^2. \tag{49}$$

The standard techniques can be used to solve the roots $\nu_1$, $\nu_2$, $\nu_3$, $\nu_4$ of the quartic equation in (44). Some roots can be complex numbers. Next, substituting these roots into (42) gives four corresponding values: $\omega_1$, $\omega_2$, $\omega_3$, $\omega_4$. Finally, $\theta_{\max}$ can be calculated using $\nu$, $\omega$ pairs and the arc-tangent function. Note that $\theta_{\max}$ are real number when the $\nu$, $\omega$ pairs are real numbers with magnitudes $\leq 1$. Pairs, which are complex numbers or have magnitudes greater than 1, should be discarded.

## ACKNOWLEDGMENT

The authors would like to thank Pakorn Ditthakit for his valuable comments and suggestions and also would like to thank Sarayoot Nakrod and Saran Wankarem for their assistance on experimentation.

## REFERENCES

[1] A. Chantaveerod, K. Woradit, A. D. Seagar, and T. Limpiti, "A novel algorithm to delineate surface water paths on digital elevation model image with boundary element method," *IEEE Access*, vol. 10, pp. 60189–60212, 2022.

[2] G. S. Dwarakish and B. P. Ganasri, "Impact of land use change on hydrological systems: A review of current modeling approaches," *Cogent Geosci.*, vol. 1, no. 1, Dec. 2015, Art. no. 1115691.

[3] L. M. Domingues, R. C. de Abreu, and H. R. da Rocha, "Hydrologic impact of climate change in the Jaguari river in the cantareira reservoir system," *Water*, vol. 14, no. 8, p. 1286, Apr. 2022.

[4] R. Martínez-Retureta, M. Aguayo, N. J. Abreu, A. Stehr, I. Duran-Llacer, L. Rodríguez-López, S. Sauvage, and J.-M. Sánchez-Pérez, "Estimation of the climate change impact on the hydrological balance in basins of south-central Chile," *Water*, vol. 13, no. 6, p. 794, Mar. 2021.

[5] T. Cui, T. Yang, C.-Y. Xu, Q. Shao, X. Wang, and Z. Li, "Assessment of the impact of climate change on flow regime at multiple temporal scales and potential ecological implications in an Alpine river," *Stochastic Environ. Res. Risk Assessment*, vol. 32, no. 6, pp. 1849–1866, Jun. 2018.

[6] C.-Y. Xu, "Climate change and hydrologic models: A review of existing gaps and recent research developments," *Water Resour. Manage.*, vol. 13, pp. 369–382, Oct. 1999.

[7] T. M. Ferreira and P. P. Santos, "An integrated approach for assessing flood risk in historic city centres," *Water*, vol. 12, no. 6, p. 1648, Jun. 2020.

[8] Y. Yin, S. Jiang, C. Pers, X. Yang, Q. Liu, J. Yuan, M. Yao, Y. He, X. Luo, and Z. Zheng, "Assessment of the spatial and temporal variations of water quality for agricultural lands with crop rotation in China by using a HYPE model," *Int. J. Environ. Res. Public Health*, vol. 13, no. 3, p. 336, Mar. 2016.

[9] Z. Akdogan and B. Güven, "Assessing the sensitivity of SWMM to variations in hydrological and hydraulic parameters: A case study for the city of Istanbul," *Global NEST J.*, vol. 18, no. 4, pp. 831–841, 2016.

[10] Z. Li, T. Yang, C.-Y. Xu, P. Shi, B. Yong, C.-S. Huang, and C. Wang, "Evaluating the area and position accuracy of surface water paths obtained by flow direction algorithms," *J. Hydrol.*, vol. 583, Apr. 2020, Art. no. 124619.

[11] C. Li, Z. Fan, Z. Wu, Z. Dai, L. Liu, and C. Zhang, "Methodology of sub-catchment division considering land uses and flow directions," *ISPRS Int. J. Geo-Inf.*, vol. 9, no. 11, p. 634, Oct. 2020.

[12] J. L. Mesa-Mingorance and F. J. Ariza-López, "Accuracy assessment of digital elevation models (DEMs): A critical review of practices of the past three decades," *Remote Sens.*, vol. 12, no. 16, p. 2630, Aug. 2020.

[13] D. Manune, *Digital Elevation Model. Technologies and Applications: The DEM Users Manual*. Bethesda, MD, USA: American Society for Photogrammetry and Remote Sensing, 2007.

[14] N. Khalid, M. A. Halim, and S. N. A. Shahimi, "A comparative study of delineated watersheds using ASTER and SRTM in Johor, Malaysia," *Int. J. Geospatial Environ. Res.*, vol. 8, no. 2, pp. 1–12, 2021.

[15] D. Tapete, A. Traviglia, E. Delpozzo, and F. Cigna, "Regional-scale systematic mapping of archaeological mounds and detection of looting using COSMO-SkyMed high resolution DEM and satellite imagery," *Remote Sens.*, vol. 13, no. 16, p. 3106, Aug. 2021.

[16] S. Shin and K. Paik, "An improved method for single flow direction calculation in grid digital elevation models," *Hydrolog. Processes*, vol. 31, no. 8, pp. 1650–1661, Apr. 2017.

[17] J. Seibert and J. J. McDonnell, "Land-cover impacts on streamflow: A change-detection modelling approach that incorporates parameter uncertainty," *Hydrolog. Sci. J.*, vol. 55, no. 3, pp. 316–332, Apr. 2010.

[18] G. Blöschl et al., "Changing climate shifts timing of European floods," *Science*, vol. 357, no. 6351, pp. 588–590, 2017.

[19] I. D. Moore, R. B. Grayson, and A. R. Ladson, "Digital terrain modelling: A review of hydrological, geomorphological, and biological applications," *Hydrolog. Processes*, vol. 5, no. 1, pp. 3–30, Jan. 1991.

[20] M. C. Rulli, "A physically based watershed partitioning method," *Adv. Water Resour.*, vol. 33, no. 10, pp. 1206–1215, Oct. 2010.

[21] J. F. O'Callaghan and D. M. Mark, "The extraction of drainage networks from digital elevation data," *Comput. Vis., Graph., Image Process.*, vol. 28, no. 3, pp. 323–344, Dec. 1984.

[22] C.-Z. Qin, B.-B. Ai, A.-X. Zhu, and J.-Z. Liu, "An efficient method for applying a differential equation to deriving the spatial distribution of specific catchment area from gridded digital elevation models," *Comput. Geosci.*, vol. 100, pp. 94–102, Mar. 2017.

[23] Q. Zhou and X. Liu, "Error assessment of grid-based flow routing algorithms used in hydrological models," *Int. J. Geographical Inf. Sci.*, vol. 16, no. 8, pp. 819–842, Dec. 2002.

[24] J. P. Walker and G. R. Willgoose, "On the effect of digital elevation model accuracy on hydrology and geomorphology," *Water Resour. Res.*, vol. 35, no. 7, pp. 2259–2268, Jul. 1999.

[25] P. Bolstad and T. Stowe, "An evaluation of DEM accuracy: Elevation, slope, and aspect," *Photogramm. Eng. Remote Sens.*, vol. 60, no. 11, pp. 1327–1332, 1994.

[26] W. Zhang and D. R. Montgomery, "Digital elevation model grid size, landscape representation, and hydrologic simulations," *Water Resour. Res.*, vol. 30, no. 4, pp. 1019–1028, Apr. 1994.

[27] X. Lin, Q. Zhang, H. Wang, C. Yao, C. Chen, L. Cheng, and Z. Li, "A DEM super-resolution reconstruction network combining internal and external learning," *Remote Sens.*, vol. 14, no. 9, p. 2181, May 2022.

[28] W. R. Dawes and D. Short, "The significance of topology for modeling the surface hydrology of fluvial landscapes," *Water Resour. Res.*, vol. 30, no. 4, pp. 1045–1055, Apr. 1994.

[29] I. D. Moore and R. B. Grayson, "Terrain-based catchment partitioning and runoff prediction using vector elevation data," *Water Resour. Res.*, vol. 27, no. 6, pp. 1177–1191, Jun. 1991.

[30] R. B. Grayson, I. D. Moore, and T. A. Mcmahon, "Physically based hydrologic modeling: 1. A terrain-based model for investigative purposes," *Water Resour. Res.*, vol. 28, no. 10, pp. 2639–2658, Oct. 1992.

[31] C. J. Maunder, "An automated method for constructing contour-based digital elevation models," *Water Resour. Res.*, vol. 35, no. 12, pp. 3931–3940, Dec. 1999.

[32] G. Menduni and V. Riboni, "A physically based catchment partitioning method for hydrological analysis," *Hydrolog. Processes*, vol. 14, nos. 11–12, pp. 1943–1962, 2000.

[33] G. Menduni, A. Pagani, M. C. Rulli, and R. Rosso, "A non-conventional watershed partitioning method for semi-distributed hydrological modelling: The package ALADHYN," *Hydrolog. Processes*, vol. 16, no. 2, pp. 277–291, 2002.

[34] G. Moretti and S. Orlandini, "Automatic delineation of drainage basins from contour elevation data using skeleton construction techniques," *Water Resour. Res.*, vol. 44, no. 5, pp. 1–15, May 2008.

[35] T. Pilz, T. Francke, and A. Bronstert, "LumpR 2.0.0: An R package facilitating landscape discretisation for hillslope-based hydrological models," *Geosci. Model Develop.*, vol. 10, no. 8, pp. 3001–3023, Aug. 2017.

[36] P. K. Kythe, *An Introduction to Boundary Element Methods*. London, U.K.: CRC Press, 1995.
[37] QGIS Development Team. (2021). *QGIS Geographic Information System*. Open Source Geospatial Foundation. [Online]. Available: http://qgis.org
[38] F. Pan, C. D. Peters-Lidard, M. J. Sale, and A. W. King, "A comparison of geographical information systems-based algorithms for computing the TOPMODEL topographic index," *Water Resour. Res.*, vol. 40, no. 6, pp. 1–22, Jun. 2004.
[39] C.-Z. Qin, L.-L. Bao, A.-X. Zhu, X.-M. Hu, and B. Qin, "Artificial surfaces simulating complex terrain types for evaluating grid-based flow direction algorithms," *Int. J. Geographical Inf. Sci.*, vol. 27, no. 6, pp. 1055–1072, Jun. 2013.

**AJALAWIT CHANTAVEEROD** was born in Hat Yai, Songkhla, Thailand. He received the bachelor's and master's degrees in electrical engineering from the Prince of Songkhla University, Thailand, in 2002 and 2004, respectively, and the Ph.D. degree in electrical engineering from Chulalongkorn University, Thailand, in 2009. He is currently a Lecturer with the School of Engineering and Technology, Walailak University, Thailand. His current research interests include the applications of boundary integral equations in engineering, numerical solution of Maxwell's equations based on Clifford algebra, and parallel algorithm for computational electromagnetics.

**KAMPOL WORADIT** (Member, IEEE) received the B.Eng. (Hons.) and Ph.D. degrees in electrical engineering from Chulalongkorn University, Thailand, in 2002 and 2010, respectively. He was a Visiting Student with the Laboratory for Information and Decision Systems, Massachusetts Institute of Technology (MIT), MA, USA, from 2007 to 2008, and was on a postgraduate research attachment with the Modulation and Coding Department, Institute for Infocomm Research, Singapore. He was a Faculty Member with the Department of Electrical Engineering, Srinakharinwirot University, Thailand, from 2010 to 2020. He is currently a Faculty Member with the Department of Computer Engineering, Chiang Mai University, Thailand. His research interests include wireless communications, the Internet of Things, and physical layer security. He received the ECTI-CON Best Paper Award, in 2019, and the Royal Golden Jubilee Scholarships from the Thailand Research Fund for his Ph.D. Program.

**ANDREW SEAGAR** (Senior Member, IEEE) received the Graduate degree from the University of Canterbury, New Zealand, in 1983. He is currently the Director of the Bachelor of Engineering Programs, Griffith University, Gold Coast Campus. He has been employed in positions of a scientist and an engineer, academic in hospitals, governmental facilities, industry, and universities in England, Australia, Canada, and Thailand. His research interest includes the solution of physical problems involving either static or dynamic electromagnetic phenomena in two or more dimensions using boundary integral approaches.

**THUNYAWAT LIMPITI** (Member, IEEE) was born in Phatthalung, Thailand, in 1982. He received the B.Eng. and M.Eng. degrees in telecommunications engineering and the D.Eng. degree in electrical engineering from the King Mongkut's Institute of Technology Ladkrabang, Bangkok, Thailand, in 2005, 2008, and 2013, respectively. He is currently an Assistant Professor with the School of Engineering and Resources, Walailak University, Thai Buri, Thailand. His current research interests include reconfigurable antenna design, microwave sensor design, and microwave techniques for dielectric properties determination.